

# **Setup and Studies of the Laser Beamline at the Compton Polarimeter at ELSA**

Florian Hinterkeuser

Masterarbeit in Physik  
angefertigt im Physikalischen Institut

vorgelegt der  
Mathematisch-Naturwissenschaftlichen Fakultät  
der  
Rheinischen Friedrich-Wilhelms-Universität  
Bonn

NOV 2015

I hereby declare that this thesis was formulated by myself and that no sources or tools other than those cited were used.

Bonn, .....  
Date

.....  
Signature

- 1. Gutachter: PD Dr. Wolfgang Hillert
- 2. Gutachterin: Prof. Dr. Jochen Dingfelder

# Contents

---

<b>1</b>	<b>Introduction</b>	<b>1</b>
<b>2</b>	<b>Compton scattering, Disk Lasers and Gaussian Optics</b>	<b>3</b>
2.1	Polarization measurement via Compton scattering . . . . .	3
2.1.1	Compton effect . . . . .	3
2.1.2	Stokes parameters . . . . .	4
2.1.3	Polarization-dependant backscattering . . . . .	6
2.1.4	Polarization measurement at ELSA . . . . .	7
2.1.5	Key Setup of a Compton Polarimeter . . . . .	9
2.2	Laser system . . . . .	10
2.2.1	Disk laser . . . . .	10
2.2.2	Second Harmonic Generation . . . . .	11
2.3	Beam Optics . . . . .	12
2.3.1	The complex beam parameter and matrix optics . . . . .	13
2.3.2	Real beam optics . . . . .	14
2.3.3	Beam characterization using the four-cuts method . . . . .	15
2.3.4	Polarization Optics . . . . .	15
<b>3</b>	<b>The Compton Polarimeter at ELSA</b>	<b>21</b>
3.1	A Brief History of the Compton Polarimeter at ELSA . . . . .	21
3.2	Setup of the Laser Beamline . . . . .	21
3.2.1	Optical Table . . . . .	21
3.2.2	Beamline . . . . .	24
3.3	Measurements of the Laser System and Beamline . . . . .	26
3.3.1	Measurement Devices . . . . .	26
3.3.2	The Complex Beam Parameter . . . . .	28
3.3.3	Laser Performance Tests . . . . .	29
3.3.4	The Focusing Optics . . . . .	36
3.3.5	Measurements of the Adjusted Beam . . . . .	38
3.4	Polarization Measurement Station . . . . .	44
<b>4</b>	<b>Summary and Outlook</b>	<b>47</b>
	<b>Bibliography</b>	<b>49</b>
	<b>List of Figures</b>	<b>51</b>
	<b>List of Tables</b>	<b>53</b>



## Introduction

---

The Physics Institute of Bonn University operates the 3.2 GeV electron stretcher accelerator ELSA since 1987. The ELSA facility, depicted in Fig. 1.1, is a three-staged accelerator complex, following a typical scheme: The first stage consists of one of two linear accelerators, either LINAC1 or LINAC2. The LINAC2 accelerates the 50 keV electron beam provided by either a thermal or polarized electron source to up to 26 MeV. The electron beam is then injected into the second stage, the booster synchrotron [1]. After the acceleration of the electron beam to typically 1.2 GeV, the beam is extracted into the stretcher ring and subsequently ramped to the desired final energy. Afterwards, the electron beam is extracted to one of the two experimental setups. The two hadron physics experiments at ELSA, BGO-OD and Crystal Barrel, contribute to the exploration of the subnuclear structure of matter within the Collaborative Research Center Transregio 16 (CRC TRR16) by studying baryonic resonances.

These studies require double polarization experiments, where a target consisting of polarized hadrons is irradiated with polarized photons obtained from the electron beam via bremsstrahlung. In this setup, circularly polarized photons can only be produced by polarized electrons. Thus, the electron beam's degree of polarization is essential for these experiments. As of now, there are two setups allowing for polarization measurements. A Mott polarimeter at the polarized electron source and a Møller polarimeter, integrated in the tagging system. Both polarimeters are based on scattering the electrons off a solid state target.

Since none of these offers any insights into depolarizing effects in ELSA, such as the crossing of depolarizing resonances during the energy ramp, the installation of an additional polarimeter is supported by the instrumentation development project D.2 of the CRC TRR16. The polarization measurement is based on the Compton effect.

First conceptions for such a polarimeter at ELSA date back to 1998 [2]. A Compton polarimeter offers the possibility to measure the electron beam's degree of polarization in the stretcher ring, without leading to significant beam loss. Thus, depolarizing effects, e.g. during acceleration, may be studied. This would offer the possibility to study the acceleration process at ELSA<sup>2</sup> with respect to the beam's degree of polarization, leading to an optimized accelerator operation. Eventually, the experiments could be provided with a maximum degree of electron polarization. Compton polarimetry is further expected to deliver more accurate polarization measurement results in a shorter amount of time compared to Moeller polarimetry.

This work describes the setup and characterization of one main backbone of the Compton polarimeter at ELSA: the optical beamline. This beamline contains the photon source, beam shaping optics and a measurement station for photon polarization measurements.

---

<sup>2</sup> Beam accumulation in the stretcher ring, accelerating to the desired energy and extraction to the target.

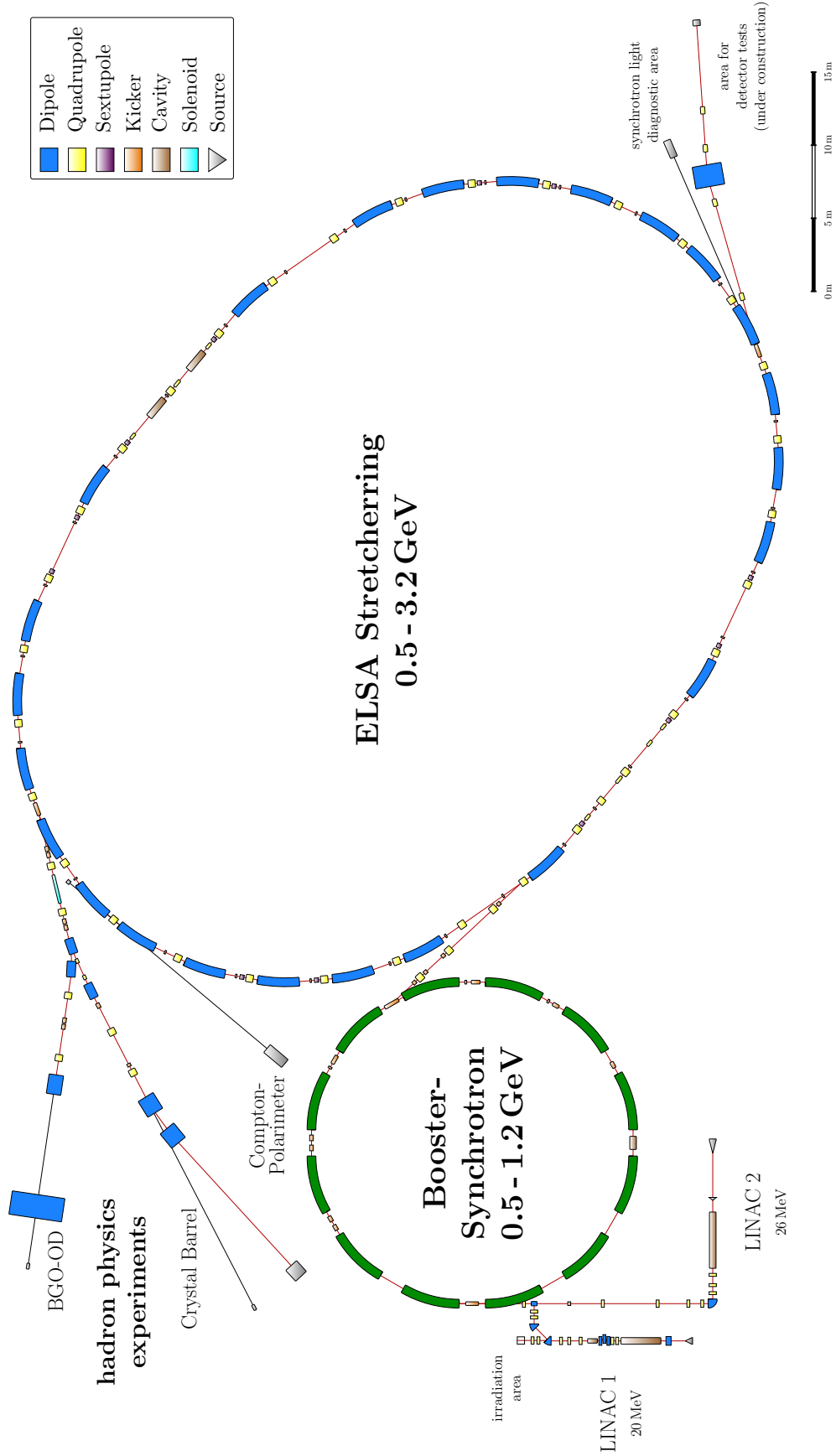


Figure 1.1: Schematics of the Electron Stretcher Accelerator ELSA.

# Compton scattering, Disk Lasers and Gaussian Optics

## 2.1 Polarization measurement via Compton scattering

### 2.1.1 Compton effect

A mathematical description of the scattering between photons and charged particles was first derived by A.H. Compton [3] from Thomson scattering, the so called *Compton scattering*. Here, photons are treated as particles with energy  $E$  and momentum  $\vec{p}$  defined using the initial wavenumber  $\vec{k}_i$

$$E = \hbar c |\vec{k}_i| \quad \vec{p} = \hbar \vec{k}_i. \quad (2.1)$$

The collision of a photon of wavenumber  $k_i$  with an electron at rest will result in the final wavenumber

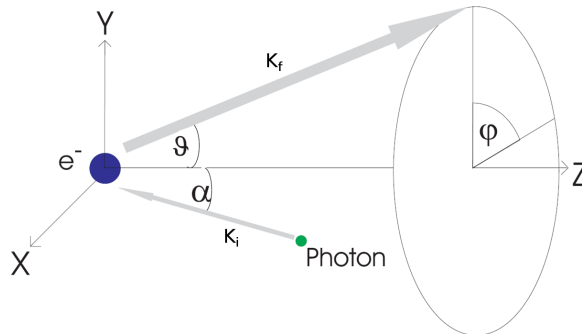


Figure 2.1: Nomenclature of Compton scattering [4].

$k_f$  given in the laboratory frame [5]:

$$k_f = \frac{1}{1 - \cos \vartheta + \frac{1}{k_i}}, \quad (2.2)$$

with the nomenclature from Fig. 2.1. From now on, parameters in the electron's rest frame are denoted  $k_i^*$ ,  $k_f^*$  etc.. To describe the scattering of photons off the relativistic electrons in ELSA in the laboratory frame, the following steps are required:

1. Lorentz transformation of the photon's four-vector into the electron's rest frame.

2. Compton scattering off an electron at rest according to the angle dependant cross-section given in the rest frame of the electron.
3. Lorentz transformation of the photon's and electron's four-vector back into the laboratory frame.

A general derivation of the Lorentz transformation can be found in [5]. Using the normalized wave number  $K = \frac{\hbar k}{m_e c}$  and assuming the electrons to move in the  $z$ -direction, transforming a photon with an incident angle  $\alpha$  yields

$$K_i^* = K_i \cdot \gamma(1 + \beta \cos \alpha) \quad (2.3)$$

$$\sin \alpha^* = \frac{\sin \alpha}{\gamma(1 + \beta \cos \alpha)}. \quad (2.4)$$

Where the Lorentz parameters  $\beta$  and  $\gamma$  are defined as

$$\beta = \frac{v}{c} \quad \gamma = \sqrt{\frac{1}{1 - \beta^2}}. \quad (2.5)$$

Assuming small incident angles  $\alpha$ , i.e. almost head on collision, this yields

$$K_i^* \approx 2\gamma K_i \quad \sin \alpha^* \approx \frac{\sin \alpha}{2\gamma}. \quad (2.6)$$

It follows that the boosted photon incident angle for ultra relativistic electrons can be neglected compared to the electron's trajectory.

The cross section  $\sigma$  of the Compton process is energy dependant. For the scattering of 30 keV photons off a free electrons, scattering in the forward direction is favoured, as can be seen in Fig. 2.2. If the photon is now scattered at an angle  $\vartheta^*$ , the corresponding final  $K_f$  is given by

$$K_f^* = \frac{1}{1 - \cos \vartheta^* + \frac{1}{K_i^*}}. \quad (2.7)$$

Assuming backscattering of the photon, i.e.  $\vartheta^* \rightarrow 0^\circ$ , and  $K_i^* \ll 1$ , the final wavenumber is obtained from

$$K_f^* \approx K_i^*. \quad (2.8)$$

From a Lorentz-Boost back into the laboratory frame, the final wavenumber  $k_f$  and scattering angle  $\vartheta$  is obtained:

$$K_f \approx 2\gamma K_f^* \quad \sin \vartheta \approx \frac{\sin \vartheta^*}{2\gamma}. \quad (2.9)$$

In the laboratory frame, most photons are backscattered at small angles.

This treatment of Compton scattering does not distinguish between polarized or unpolarized electrons and photons. In the following, the impact of the photons' degree of polarization will be considered. Since this treatment requires knowledge of the Stokes parameters, they will be introduced first.

### 2.1.2 Stokes parameters

The Stokes parameters are a set of four values, e.g.  $S_0, S_1, S_2$  and  $S_3$ , describing the polarization state of electromagnetic radiation. Given the transverse field amplitudes  $E_X$  and  $E_Y$  and the relative phase  $\delta$

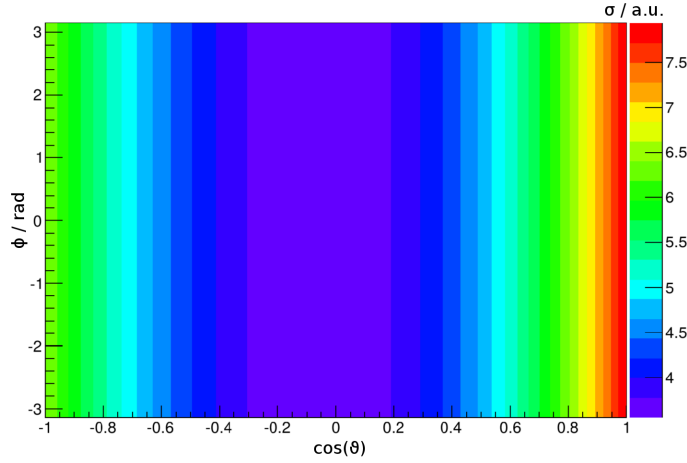


Figure 2.2: Cross section for scattering a 30 keV photon off a free electron in the electron's rest frame.<sup>1</sup>

between  $E_X$  and  $E_Y$ , the Stokes parameters are

$$\vec{S} = \begin{pmatrix} S_0 \\ S_1 \\ S_2 \\ S_3 \end{pmatrix} = \begin{pmatrix} E_X^2 + E_Y^2 \\ E_X^2 - E_Y^2 \\ 2E_X E_Y \cdot \cos(\delta) \\ 2E_X E_Y \cdot \sin(\delta) \end{pmatrix}. \quad (2.10)$$

In the case of completely polarized light, the Stokes parameters fulfill the relation

$$S_0 = \sqrt{S_1^2 + S_2^2 + S_3^2}. \quad (2.11)$$

By scaling the Stokes parameters with the total incident intensity  $S_0$ , the degree of polarization  $P_\gamma$  is determined by

$$P_\gamma = \frac{\sqrt{S_1^2 + S_2^2 + S_3^2}}{S_0}. \quad (2.12)$$

This relation allows for a simple measurement of polarization, only requiring a polarization filter.

In the case of circularly polarized light, the Stokes vectors follow as

$$\vec{S}_{\sigma^+} = \begin{pmatrix} 1 \\ 0 \\ 0 \\ 1 \end{pmatrix} \quad \vec{S}_{\sigma^-} = \begin{pmatrix} 1 \\ 0 \\ 0 \\ -1 \end{pmatrix}. \quad (2.13)$$

Any optical component's influence on a polarized photon beam can be characterized using a so called Mueller Matrix  $M_i$ . Similar to matrix optics, it holds for any optical system

$$\vec{S}_0 = M_n \cdot (M_{n-1} \cdot \dots \cdot (M_1 \cdot \vec{S}_i)). \quad (2.14)$$

In section 2.3.4, examples for Mueller matrices are given.

<sup>1</sup> Courtesy of R.Koop

### 2.1.3 Polarization-dependant backscattering

In 1954, the polarization-dependant differential cross section for scattering photons off electrons was published by F.W. Lipps and H.A. Tolhoek [6], expressing the photon polarization using Stokes parameters. Assuming the initial degree of polarization of the photon  $\vec{S}$  and electron  $\vec{P}$  are known, and using the nomenclature represented in Fig. 2.1, the cross differential section follows as

$$\frac{d\sigma}{d\Omega}(\vec{S}, \vec{P}) = \Sigma_0 + \Sigma_1(S_1) + \Sigma_2(S_3, \vec{P}). \quad (2.15)$$

Using the classical electron radius  $r_e$ , the single terms are

$$\Sigma_0 = C(1 + \cos^2 \vartheta^* + (K_i^* - K_f^*)(1 - \cos \vartheta^*)) \quad (2.16)$$

$$\Sigma_1(S_1) = C \cdot S_1 \sin^2 \vartheta^* \quad (2.17)$$

$$\Sigma_2(S_3, \vec{P}) = -C \cdot S_3(1 - \cos \vartheta^*) (\vec{K}_i^* \cos \vartheta^* + \vec{K}_f^*) \cdot \vec{P} \quad (2.18)$$

$$C = \frac{r_e^2}{2} \cdot \left( \frac{K_f^*}{K_i^*} \right)^2. \quad (2.19)$$

$\Sigma_0$  does not depend on polarization states,  $\Sigma_1$  depends on the incident photon's polarization only.  $\Sigma_2$  is the only term depending on the electron's longitudinal and transverse polarization. The electron polarization's influence on the cross section can be expressed as [2]

$$\Sigma_2(S_3, \vec{P}) = S_3 P_Z \cdot \Sigma_{2Z} \cdot \sin \varphi^* + S_3 P_S \cdot \Sigma_{2S}, \quad (2.20)$$

using

$$\Sigma_{2Z} = -CK_f^* \sin \vartheta^* (1 - \cos \vartheta^*), \quad (2.21)$$

$$\Sigma_{2S} = -C(1 - \cos \vartheta^*) (K_f^* + K_i^*) \cos \vartheta^*. \quad (2.22)$$

A transverse electron polarization thus leads to a  $\sin \varphi$ -modulation of the cross section. For right- and left-handed 30 keV photons, the modulated cross section in the electron's rest frame is shown in Fig. 2.3.

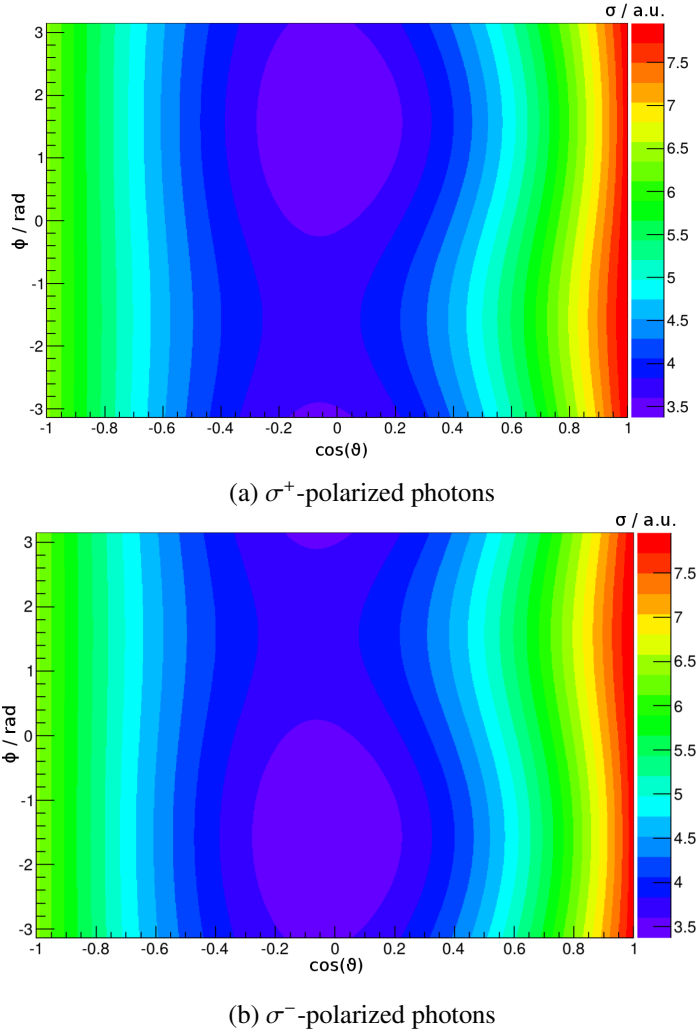


Figure 2.3: The cross section for Compton scattering in the electron's rest frame for circularly polarized photons and linearly polarized electrons.<sup>1</sup>

This modulation can be measured by an appropriate detector. The modulation depth  $M = \frac{\Sigma_{ZZ}}{\Sigma_0} \cdot S_3 P_Z$  depends on the polar angle  $\vartheta^*$  and is proportional to the incident photon energy, refer to Fig. 2.4, thus photons of a short wavelength are desired. Since  $M$  is proportional to  $P_Z$  and  $S_3$ , the transverse electron polarization can be obtained by measuring the modulation depth, assuming the photon polarization is known.

#### 2.1.4 Polarization measurement at ELSA

For Compton Polarimetry at ELSA, a circularly polarized  $S_3 \neq 0$  photon beam is brought to collision with the partially polarized electron beam  $P_Z \neq 0$ . The modulated Compton scattering cross section for a polarized electron and photon beam, as seen in Figs. 2.3, causes a spatial asymmetry in the intensity profile of the backscattered photons. When switching the photon polarization from  $\sigma^\pm$  to  $\sigma^\mp$ , thus changing the sign of  $S_3$ , this asymmetry results in a vertical shift  $\Delta x$  of the intensity profile's center

<sup>1</sup> Courtesy of R.Koop

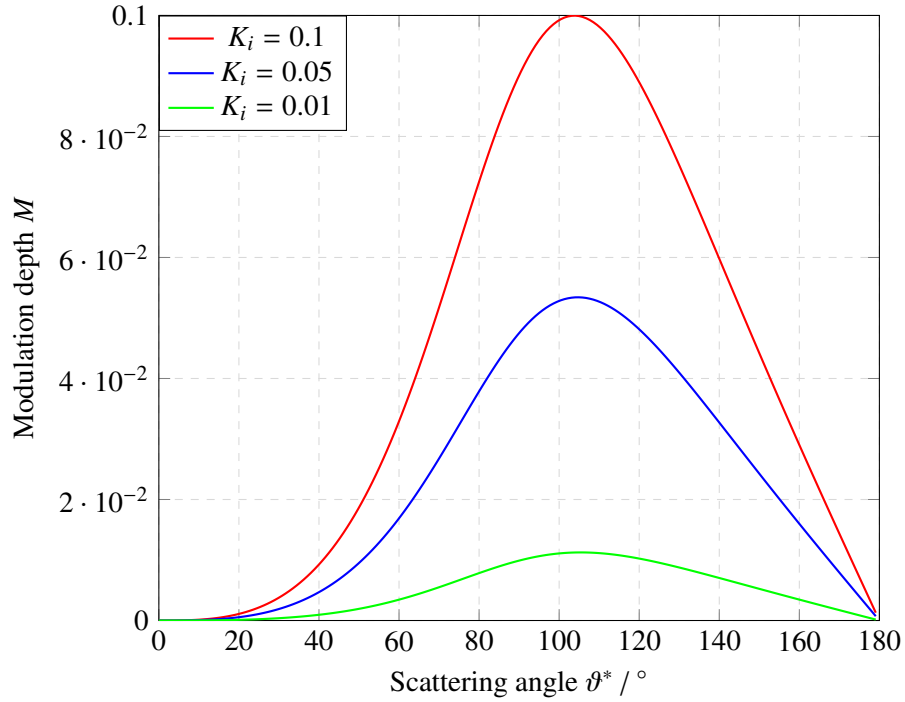


Figure 2.4: Modulation depth in dependence of the scattering angle  $\theta^*$  for different incident photon energies.

of mass. This shift turns out to be directly proportional to  $S_3$  and  $P_Z$ . Therefore, if  $S_3$  is known, the measurement of  $\Delta x$  will provide the desired electron polarization degree:

$$P_Z = \frac{\Delta x}{C \cdot S_3}, \quad (2.23)$$

with  $C$  being a scaling factor obtained by a calibration measurement.

This factor  $C$  represents the measurable center of mass shift for the maximum degrees of polarization achievable. It can be determined using the Sokolov-Ternov effect [7]. This effect describes the self-polarization of an electron beam in a storage ring caused by the emission of synchrotron radiation in transverse magnetic fields. The photons are emitted while conserving or inverting the electron's spin component parallel to the transverse magnetic field. A final state with the spin antiparallel to the magnetic field is favored, thus leading to a transverse electron polarization. The degree of electron polarization at a time  $t$  is then given by [7]

$$P(t) = P_\infty \left(1 - \exp\left(-\frac{t}{\tau}\right)\right), \quad (2.24)$$

with the asymptotic limit  $P_\infty \approx 92.4\%$  and the time constant  $\tau = \frac{2.828 \cdot 10^{21}}{\gamma^5}$  s, with the Lorentz factor  $\gamma$ . At ELSA, the time constant  $\tau$  is in the order of 5 minutes for beam energies of 3.2 GeV. This self-polarization of the electron beam offers an opportunity to calibrate the polarimeter for following measurements.

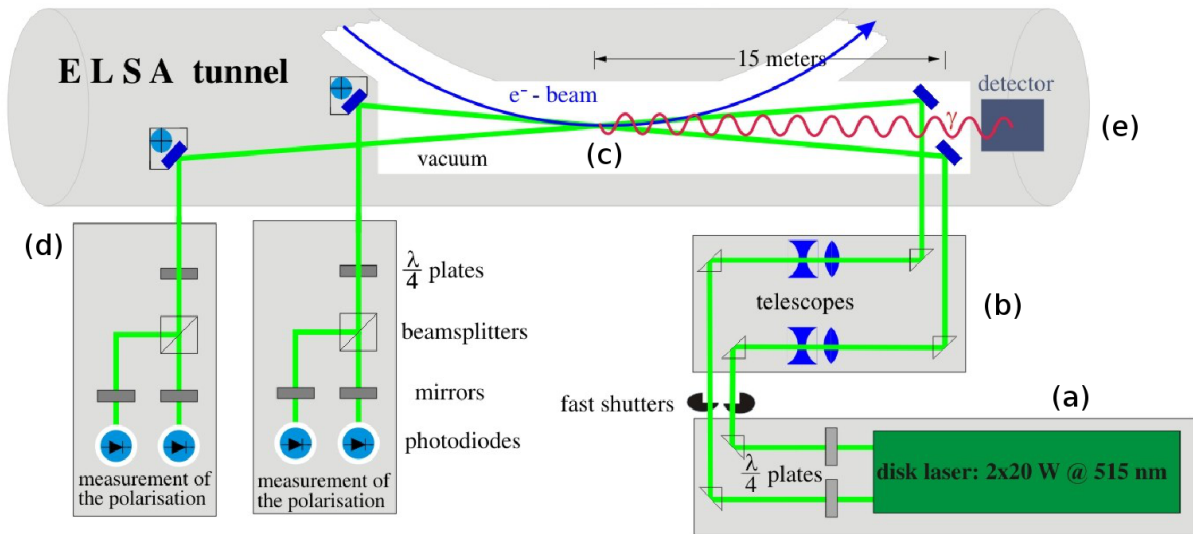


Figure 2.5: Design of the Compton polarimeter at ELSA with key components: A laser system (a), beam shaping optics (b), beamline with the interaction region (c), photon polarization measurement station (d) and a detector system (e) for the measurement of backscattered  $\gamma$ -photons. This sketch is not true to scale.<sup>1</sup>

### 2.1.5 Key Setup of a Compton Polarimeter

In order to perform the electron polarization measurement at ELSA, a setup as shown in Fig. 2.5 is used. The key components of this setup are:

- **The photon source**

The photon source has to provide a high intensity, monochromatic photon beam, which is accomplished by using a laser. The laser system used provides linearly polarized photons with a wavelength of 515 nm. The concept of this laser is introduced in section 2.2.1, studies of the laser system are presented in sections 3.3.2 and 3.3.3. In order to describe the properties and propagation of the laser beams, the concept of Gaussian optics introduced in section 2.3 is used.

- **Beam-shaping optics**

The beam-shaping optics is responsible for providing beam of high photon density in the interaction region of the Compton polarimeter. Thus, the photon beam has to be focused into the 16 m distant QD<sup>2</sup> 25 magnet. The telescope optics installed is treated in section 3.3.4. In the interaction region, the photon beam width should be smaller than the electron beam width in order to maximize the event rate. In order to maximize the center-of-mass shift of the backscattered photons, the degree of circular polarization has to be maximized. This is done by using quarter-wave plates, that convert the linearly polarized laser light into circularly polarized light. The resulting properties of the photon beams in the interaction region are presented in section 3.3.5.

- **The photon polarization measurement station**

The polarization measurement station is responsible for determining the photon beam polarization needed for the calculation of  $P_Z$  according to 2.23. It uses a second set of quarter-wave plates and polarizing beamsplitters. The operation principle and setup at ELSA is treated in section 3.4.

<sup>1</sup> Courtesy of W. Hillert

<sup>2</sup> Horizontally defocusing quadrupole

- **Detector system**

A silicon detector measures the shift in the center of mass of the backscattered photons for  $\sigma^+$ - and  $\sigma^-$ -polarized light. The detector system's FPGA<sup>1</sup>-board is responsible for controlling the measurement process at the Compton polarimeter at ELSA.

## 2.2 Laser system

### 2.2.1 Disk laser

The monochromatic photons used in the polarimeter are provided by a frequency doubled Yb:YAG<sup>2</sup> disk laser<sup>3</sup> with a design output power of  $2 \times 20$  W at a wavelength of 515 nm. A disk laser design was chosen, since the high photon densities in modern laser systems can lead to issues due to thermal stress of the optical components. Especially in solid state lasers, this can cause unwanted side effects like thermal lensing<sup>4</sup>. The amount of heat induced into the gain medium can only be lowered by decreasing the pumping power. In order to achieve higher output powers while maintaining the beam quality, the thermal properties of the laser's gain medium had to be improved to withstand higher power densities.

A possible solution was presented by A. Giesen [8]. In a disk laser setup, the gain medium is shaped as a thin disk<sup>5</sup> instead of a block or rod. The disk is mounted on a heat sink and pumped by high-power diode lasers. Since the distance between the disk and heat sink is very small, an efficient cooling of the gain medium is possible. The thermal gradient is oriented parallel to the optical axis of the resonator. If the disk is thinner than the radius of the pumping laser beam, the thermal flow can be assumed to be one dimensional [8]. Due to the efficient cooling of the laser disk, an active medium like Yb:YAG can

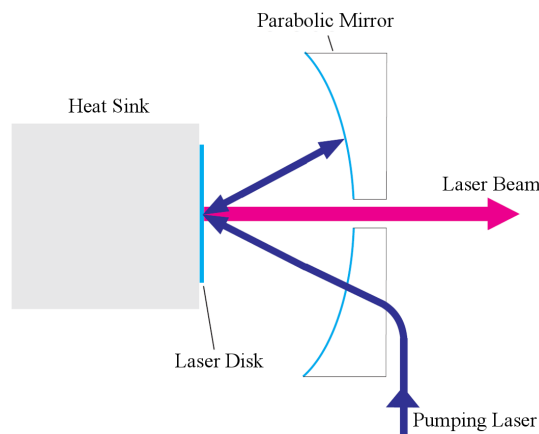


Figure 2.6: Concept of a disk laser unit. [4]

be utilized, which requires high pumping densities. It offers several advantages over the wide-spread Nd:YAG<sup>6</sup> lasers [8]:

<sup>1</sup> Field-programmable gate array

<sup>2</sup> Ytterbium doped yttrium aluminum garnet

<sup>3</sup> Elektronik Laser Systems ELS MonoDisk Gemini 20

<sup>4</sup> Due to the high power densities, the geometrical shape or refractive index of a material can change. This can have a significant impact on the beam properties, even leading to the destruction of the gain medium.

<sup>5</sup> The laser disks of the MonoDisk Gemini are  $240 \mu\text{m}$  thick.

<sup>6</sup> Neodymium-doped yttrium aluminium garnet

- higher possible concentrations of Yb allow for higher gain in a comparable volume.
- an absorption bandwidth of 10 nm at 940 nm compared to 0.8 nm for Nd:YAG.
- longer lifetime of 0.96 ms for the excited state, compared to 0.24 ms for Nd:YAG.
- reduced losses due to missing excited state absorption.
- higher overall efficiency of 91 % compared to 76 % for Nd:YAG.

The rear side of the laser disk is covered with a reflective coating for the pumping wavelength (940) nm as well as the laser wavelength (1030) nm. The principle setup is shown in Fig. 2.6. Since the interaction length is rather small, the pumping beam has to pass the disk several times. This is achieved by a special arrangement of mirrors and prisms. The laser disk consequently is gain medium and resonator at once.

The MonoDisk Gemini laser system contains two disk laser units in a double-folded X-configuration as shown in Fig. 2.7.

Using spherical mirrors in this configuration, focal points in the laser disks as well as in the SHG<sup>1</sup>-unit are obtained without using additional lenses. In order to reduce the bandwidth  $\Delta f$  of the resonator, a Fabry-Perot etalon as well as a Lyot filter are each used. In this case, a bandwidth of 2 GHz is achieved.

### 2.2.2 Second Harmonic Generation

The desired wavelength of 515 nm is obtained by frequency conversion [9]. For low intensities, the polarization  $P$  in a medium depends linearly on the EM wave's electric field strength  $E$ . The polarization  $P$  is given by a series

$$P = \varepsilon_0 \sum_n \chi^{(n)} E^n, \quad (2.25)$$

with the vacuum permittivity  $\varepsilon_0$  and the electric susceptibility  $\chi^{(n)}$ . For high intensities, higher order terms cannot be neglected. In the case of  $n = 2$ , the polarization is given by

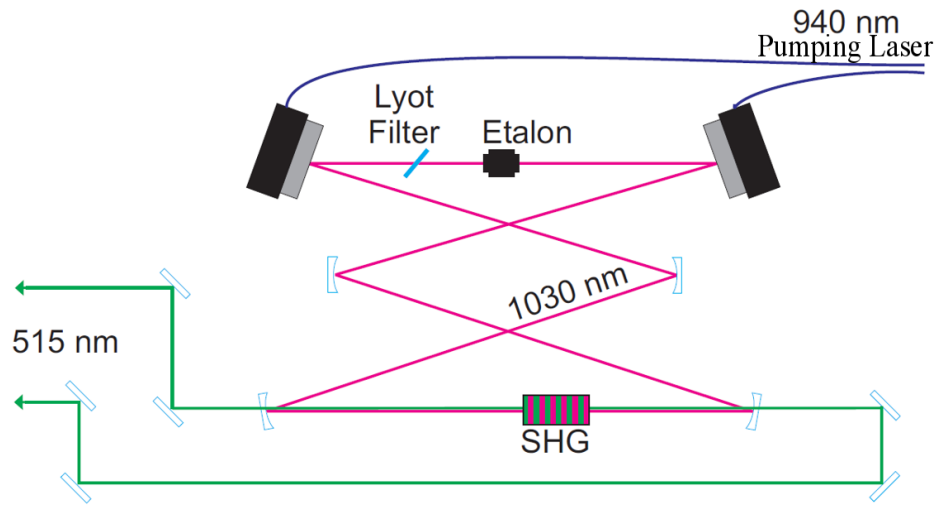
$$P^{(2)} = \varepsilon_0 \chi^{(2)} \cdot \frac{E_0^2}{2} - \cos(2\omega t) \cdot \varepsilon_0 \chi^{(2)} \cdot \frac{E_0^2}{2}, \quad (2.26)$$

for an external excitation frequency  $\omega$ . The second term gives the fraction of the Hertzian dipoles oscillating with  $2\omega$ , thus half the wavelength. This results in a partial frequency conversion of the incident light from  $\omega$  to  $2\omega$ . To prevent destructive interference of the second harmonic, it has to be phase-matched, i.e. the exciting and resulting wave have to be in phase.

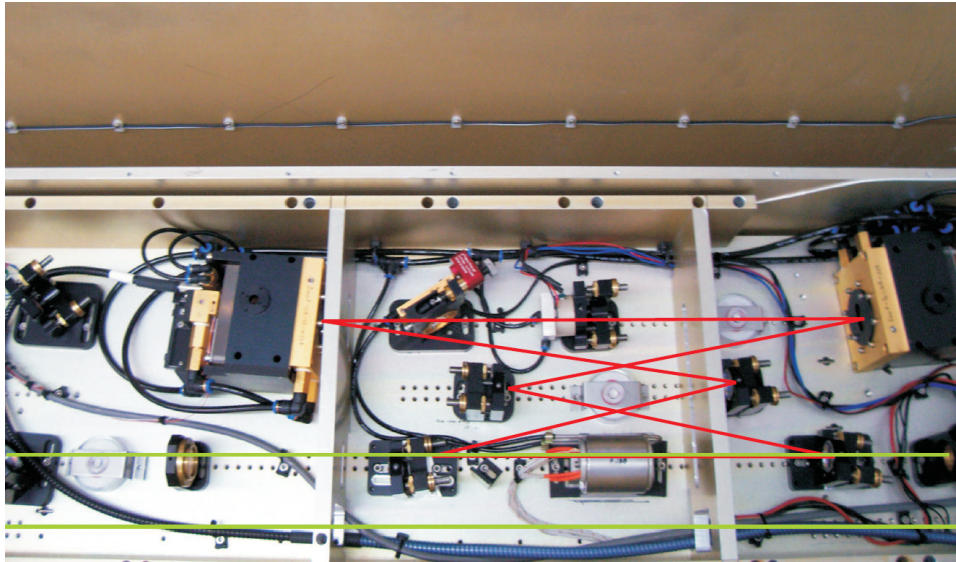
Second harmonic generation as an even-order nonlinear effect, is only allowed in mediums without inversion symmetry. In addition, the material in question has to be chemically and thermally stable due to the extreme conditions in the resonator. In case of the MonoDisk Gemini, the SHG crystal consists of lithium triborate,  $\text{LiB}_3\text{O}_5$ , see [10] for details.

Phase-matching in LBO can be achieved in two different ways. One possibility is the so-called angle tuning, i.e. ensuring  $n_\omega = n_{2\omega}$  by twisting the crystal. A more simple approach is temperature tuning: Since the refractive index of birefringent crystals like LBO is strongly temperature dependant, the phase-matching condition  $n(T)_\omega = n(T)_{2\omega}$  can be ensured by heating the crystal to an adequate temperature. Temperature tuning is however an additional source of thermal stress for the SHG crystal, which can cause damage to the crystal. Before 2013, the LBO crystal in the existing laser system had to be heated up to a temperature of 213 °C. Since 2013, phase-matching is achieved by angle tuning at room temperature.

<sup>1</sup> second-harmonic-generation



(a) Sketch of the MonoDisk Gemini resonator with a second-harmonic-generation unit.



(b) Pictured interior of the ELS MonoDisk Gemini with the sketched beam propagation.

Figure 2.7: Interior setup of the ELS MonoDisk Gemini 20 disk laser. [4]

## 2.3 Beam Optics

The laser beams have to be focused in the interaction region to maximize the scattering rate. A model accurately describing laser beam propagation and the impact of optical elements on a laser beam is needed in order to find an appropriate set of optical elements. The concept of modelling the laser beam with Gaussian functions proved to be adequate. These gaussian functions are solutions to the paraxial Helmholtz equations. The complex electrical field amplitude in a medium with refractive index  $n$  is given by

$$E_{\text{Gauss}}(z, r, t) = \frac{|E_0|}{1 - i\frac{z-\lambda}{\omega_0^2 n \pi}} \cdot \exp\left(-\frac{r^2/\omega_0^2}{1 - \frac{iz\lambda}{\omega_0^2 n \pi}}\right), \quad (2.27)$$

with the wavelength  $\lambda$ , the direction of propagation  $z$  and distance from the center axis  $r$ . The focus  $\omega_0$  is defined to be at  $z_0 = z = 0$ . For a detailed derivation, see [11].

Although this description is more complex compared to geometrical optics, some assumptions of the latter still apply:

1. The beams have a small divergence, thus the paraxial approximation is justified.
2. Any medium is assumed to be homogeneous.
3. Snell's law applies.

The beam radius is defined as the distance from the beam's center, at which the intensity has dropped to  $1/e^2$  of the maximum value. For a Gaussian beam, it is completely defined by the focal beam radius  $\omega_0$ , the longitudinal distance to the focal point  $z$ , the wavelength  $\lambda$  and the refractive index  $n$  by

$$\omega(z) = \omega_0 \cdot \sqrt{1 + \left(\frac{z\lambda}{\omega_0^2 n \pi}\right)^2}. \quad (2.28)$$

Some additional useful beam parameters, also shown in Fig. 2.8, are:

- **Rayleigh-length  $z_R$**

The Rayleigh length is defined as the distance from the waist, at which the beam width increases by  $\sqrt{2}$ :

$$z_R = \frac{n\pi\omega_0^2}{\lambda}.$$

Within  $\pm z_R$  around the waist, the beam wavefronts can be assumed to be parallel. This range is called the *depth of focus* of the laser beam.

- **Radius of curvature  $R(z)$**

The radii of the wavefronts comprising the beam at a position  $z$  is given by the radius of curvature as follows:

$$R(z) = z \cdot \left(1 + \left(\frac{z_R}{z}\right)^2\right). \quad (2.29)$$

- **Far-field divergence angle**

For values  $z \gg z_R$ , the beam radius increases linearly. This can be described using the far-field divergence angle  $\Theta$ :

$$\Theta = \frac{\omega_0}{z_R}. \quad (2.30)$$

### 2.3.1 The complex beam parameter and matrix optics

In order to analyse the propagation of a Gaussian beam, one can encode information about the beam waist  $\omega_0$  and radius of curvature  $R(z)$  into the complex beam parameter  $q(z)$ . It is defined as

$$q(z) = \left(\frac{1}{R(z)} - \frac{i\lambda}{\pi \cdot n \cdot \omega(z)^2}\right)^{-1} = z + iz_R. \quad (2.31)$$

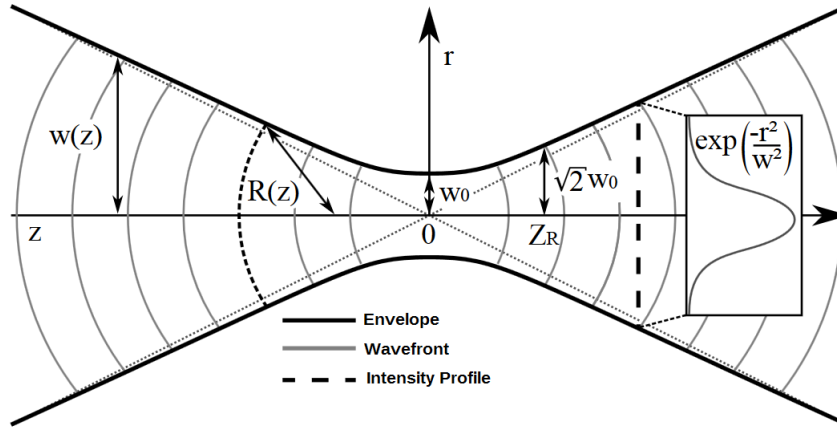


Figure 2.8: Parameters of a Gaussian beam

Using this beam parameter, one can perform a ray transfer matrix analysis similar to geometric optics. In this formalism, any linear optical element can be described as a 2x2 matrix

$$M = \begin{pmatrix} A & B \\ C & D \end{pmatrix}, \quad (2.32)$$

using typical matrices known from geometrical optics. A system of  $n$  optical elements is described by the matrix  $M_{\text{tot}}$

$$M_{\text{tot}} = \begin{pmatrix} A_{\text{tot}} & B_{\text{tot}} \\ C_{\text{tot}} & D_{\text{tot}} \end{pmatrix} = \begin{pmatrix} A_n & B_n \\ C_n & D_n \end{pmatrix} \cdot \begin{pmatrix} A_{n-1} & B_{n-1} \\ C_{n-1} & D_{n-1} \end{pmatrix} \cdot \dots \cdot \begin{pmatrix} A_1 & B_1 \\ C_1 & D_1 \end{pmatrix}. \quad (2.33)$$

The complex beam parameter  $q(R, \omega)$  at a point after passing through an optical system with the transfer matrix  $M_{\text{opt}}$  is obtained by

$$q_f(z_f, z_{R,f}) = \frac{A_{\text{opt}} \cdot q_i(z_i, z_{R,i}) + B_{\text{opt}}}{C_{\text{opt}} \cdot q_i(z_i, z_{R,i}) + D_{\text{opt}}}. \quad (2.34)$$

The indices  $i, f$  denote the initial and final positions  $z_i, z_f$  and Rayleigh lengths  $z_{R,i}, z_{R,f}$  respectively.

### 2.3.2 Real beam optics

Up until now, laser beams were assumed to be ideal gaussian beams. As shown in [12], a laser beam consists of several Hermite-Gaussian or Laguerre-Gaussian modes. These modes are the eigenmodes of the optical resonator and typically designated  $\text{TEM}_{nm}^1$  modes. The fundamental mode, the  $\text{TEM}_{00}$ , is a radially symmetric gaussian beam. This treatment is similar to the concept of rf-cavities in accelerator physics, refer to e.g. [13].

For many applications, the fundamental  $\text{TEM}_{00}$  mode is most suited. A quantity describing the beam quality is the beam propagation factor  $M^2$ . It is defined using the beam parameters  $\omega$  and  $\Theta$  of the actual beam and an ideal Gaussian beam:

$$M^2 = \frac{\omega_{\text{real}}(z) \cdot \Theta_{\text{real}}}{\omega_{\text{Gauss}}(z) \cdot \Theta_{\text{Gauss}}} \geq 1. \quad (2.35)$$

$M^2$  can be understood as the ratio of a real beam's waist and the waist of a Gaussian beam assuming

<sup>1</sup> Transverse ElectroMagnetic

identical divergences:

$$\omega_{\text{real}}(z) = M^2 \cdot \omega_{\text{Gauss}}(z). \quad (2.36)$$

The beam's mode composition is close to a pure Gaussian beam, if  $M^2 \approx 1$ . Due to effects like thermal lenses, high beam qualities are difficult to obtain with high power laser systems. The laser used in the Compton polarimeter has a design value of  $M^2 < 1.1$ . Thus a treatment of the laser system in terms of Gaussian beams is justified.

### 2.3.3 Beam characterization using the four-cuts method

Accurate beam characterization is necessary in order to perform any calculation or adjustments concerning the Compton polarimeter's laser beamline. The concept of choice is the so called *four-cuts method*, the principle is explained in [14].

It is based on imaging the input beam using a lens with known properties. The resulting beam parameters are measured and transformed back through the lens to obtain the incident beam parameters. The distance from the beam waist to the lens and the beam width are being measured at several longitudinal positions behind the lens. Beam waist location and width are obtained using a fit function. The beam divergence is given by the beam width one focal length  $f$  behind the lens via

$$\Theta_{\text{Beam}} = \frac{2 \cdot \omega_f}{f}. \quad (2.37)$$

A distinct fit requires at least 4 data points, two for each side of the waist.

According to the ISO Standard 11146 [15], 5 data points within the rayleigh length and 5 at a distance  $z > z_R$  are required to ensure sufficient accuracy. Fig. 2.9 gives an example of the four-cuts method.

The device<sup>1</sup> that is used to measure the parameters of the laser beams uses 260 sampling points.

In the case of known wavelength  $\lambda$  and refractive index  $n$  as well as the corresponding properties of a Gaussian beam, the beam propagation factor is calculated according to equation 2.35.

### 2.3.4 Polarization Optics

#### Retardation Plate

Retardation plates are manufactured out of birefringent materials, for which the index of refraction depends on the orientation and polarization of light passing through it. These plates are obtained e.g. by cutting a birefringent crystal. The orientation of the cut is chosen so that the optic axis of the plate is parallel to the surface. Hence the ordinary axis is oriented perpendicular to the optic axis, the extraordinary axis parallel. This leads to a phase shift, or retardation, between the light components polarized perpendicular<sup>2</sup> and parallel<sup>3</sup> to the incident plane. For  $n_e < n_o$ , the extraordinary axis is called the *fast axis*, and vice versa. The exact behaviour of those plates depends on the thickness  $L$  of the plate, variation of the refractive index  $\Delta n$  and wavelength of the incident light. The phase shift between the fast axis and the slow axis is given by

$$\delta = \frac{2\pi\Delta nL}{\lambda_0}, \quad (2.38)$$

<sup>1</sup> A *ModeMaster PC*, manufactured by Coherent Inc.. See chapter 3.3.1 for details.

<sup>2</sup> *s*-polarized light

<sup>3</sup> *p*-polarized light

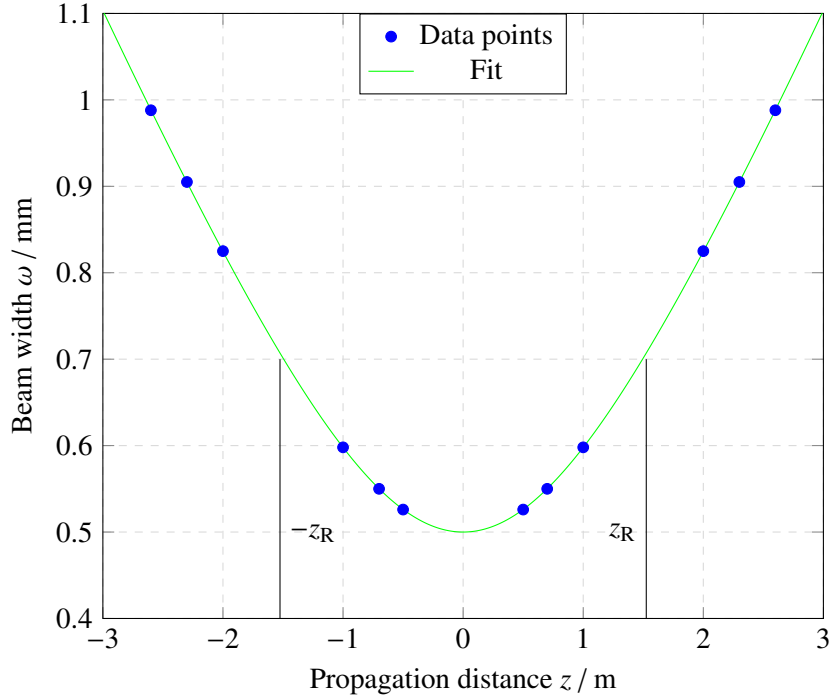


Figure 2.9: Depiction of the four-cuts method.

with the vacuum wavelength  $\lambda_0$ . The general Mueller matrix of a retardation plate is

$$M_{\text{ret}} = \begin{pmatrix} 1 & 0 & 0 & 0 \\ 0 & \cos^2 2\Theta + \cos \delta \sin^2 2\Theta & \cos 2\Theta \sin 2\Theta - \cos 2\Theta \cos \delta \sin 2\Theta & \sin 2\Theta \sin \delta \\ 0 & \cos 2\Theta \sin 2\Theta - \cos 2\Theta \cos \delta \sin 2\Theta & \cos \delta \cos^2 2\Theta + \sin^2 2\Theta & -\cos 2\Theta \sin \delta \\ 0 & -\sin 2\Theta \sin \delta & \cos 2\Theta \sin \delta & \cos \delta \end{pmatrix}. \quad (2.39)$$

$\Theta$  depicts the angle of the fast axis. The two most significant cases are  $\delta = n + \pi$ , known as an  $n$ -th order half-wave plate and  $\delta = n + \frac{\pi}{2}$ , an  $n$ -th order quarter-wave plate, for  $n \in \mathbb{N}$ . The quarter-wave plates used in the beamline are AR<sup>1</sup>-coated, zero order quartz plates. A true zero order quarter wave plate would be too thin for an effective fabrication process. Instead, it consists of two multiple-order wave plates. The retardations of these wave plates differ by exactly  $\frac{1}{4}$ . This gives the wave plate the properties of a true zero order wave plate while being much easier to produce. Assuming that the fast axis of the wave plate is oriented vertically or horizontally, the Mueller matrix reads

$$M_{\frac{\lambda}{4}} = \begin{pmatrix} 1 & 0 & 0 & 0 \\ 0 & 1 & 0 & 0 \\ 0 & 0 & 0 & \pm 1 \\ 0 & 0 & \mp 1 & 0 \end{pmatrix}. \quad (2.40)$$

<sup>1</sup> Anti-Reflective

Consider a linearly polarized light beam, tilted by  $\pm 45^\circ$ . The Stokes vector of the resulting beam is

$$\vec{S}_f = \begin{pmatrix} 1 & 0 & 0 & 0 \\ 0 & 1 & 0 & 0 \\ 0 & 0 & 0 & \pm 1 \\ 0 & 0 & \mp 1 & 0 \end{pmatrix} \cdot \begin{pmatrix} 1 \\ 0 \\ \pm 1 \\ 0 \end{pmatrix} = \begin{pmatrix} 1 \\ 0 \\ 0 \\ \mp 1 \end{pmatrix}, \quad (2.41)$$

thus leading to circularly polarized light. Similarly, if circularly polarized light passes a quarter-wave plate at an angle  $\pm 45^\circ$  towards the fast axis, the resulting light is again linearly polarized.

### Polarizing Beam Splitter

The Compton polarimeter at ELSA as well as photon polarization measurements performed during this work made use of polarizing beam splitter cubes. The polarizing beam splitter cubes used in the polarimeter consist of two glass prisms each. The vertical and horizontal electrical field components of the incident light are separated using a dielectrical coating on the boundary of both prisms. This concept exploits the higher reflectivity of the  $s$ -polarized field component at a boundary under  $45^\circ$ . By using several layers of this coating, the field components are separated. The Mueller matrices for the transmitted branches are those of a linear polarizer with horizontal or vertical transmission:

$$M_{p-/s-} = \frac{1}{2} \cdot \begin{pmatrix} 1 & \pm 1 & 0 & 0 \\ \pm 1 & 1 & 0 & 0 \\ 0 & 0 & 0 & 0 \\ 0 & 0 & 0 & 0 \end{pmatrix}. \quad (2.42)$$

Since the beamsplitters are optical contacted instead of glued together, they are comparably impervious to high power densities and thus well suited for the application in the Compton polarimeter at ELSA.

### Reflection of Polarized Light

The reflection of light at a boundary between two mediums with refractive indices  $n_1$  and  $n_2$  can be described using the fresnel equations [16]. For  $s$ - or  $p$ -polarized light, the reflectance at the boundary between two materials is given by

$$R_s = \frac{|Z_2 \cos \theta_i - Z_1 \cos \theta_t|^2}{|Z_2 \cos \theta_i + Z_1 \cos \theta_t|^2}, \quad (2.43)$$

$$R_p = \frac{|Z_2 \cos \theta_t - Z_1 \cos \theta_i|^2}{|Z_2 \cos \theta_t + Z_1 \cos \theta_i|^2}. \quad (2.44)$$

$Z = \sqrt{\frac{\epsilon}{\mu}}$  denotes the wave impedance of the respective medium,  $\theta_{i/t}$  the incident or transmission angle respectively. These angles are connected via Snell's law:

$$n_1 \sin \theta_i = n_2 \sin \theta_t. \quad (2.45)$$

For most dielectric materials  $\mu_1 = \mu_2 = \mu_0$  holds, reducing the reflectance to

$$R_s = \left| \frac{n_1 \cos \theta_i - n_2 \cos \theta_t}{n_1 \cos \theta_i + n_2 \cos \theta_t} \right|^2, \quad (2.46)$$

$$R_p = \left| \frac{n_1 \cos \theta_t - n_2 \cos \theta_i}{n_1 \cos \theta_t + n_2 \cos \theta_i} \right|^2. \quad (2.47)$$

Fig. 2.10 shows the reflectance for  $s$ - and  $p$ -polarized light respectively for a transition from air to fused

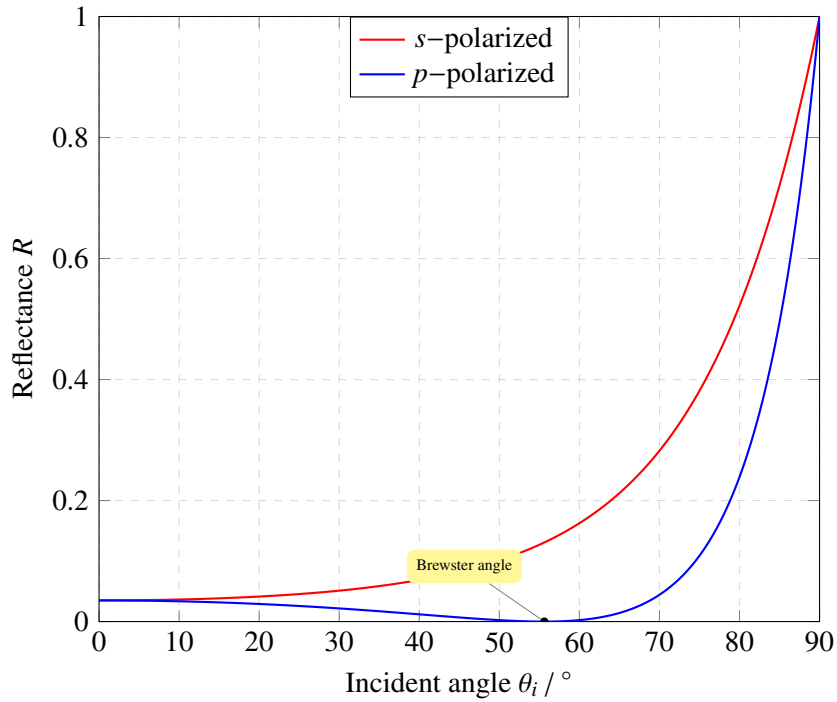


Figure 2.10: Reflectance of  $s$ - and  $p$ - polarized light at the boundary between air and fused silica, depending on the incident angle.

silica. As can be seen, the reflection coefficient for  $s$ -polarized light is usually higher. The reflectance of  $p$ -polarized light becomes 0, if the incident angle equals Brewster's angle

$$\theta_{\text{Brewster}} = \arctan \frac{n_2}{n_1}. \quad (2.48)$$

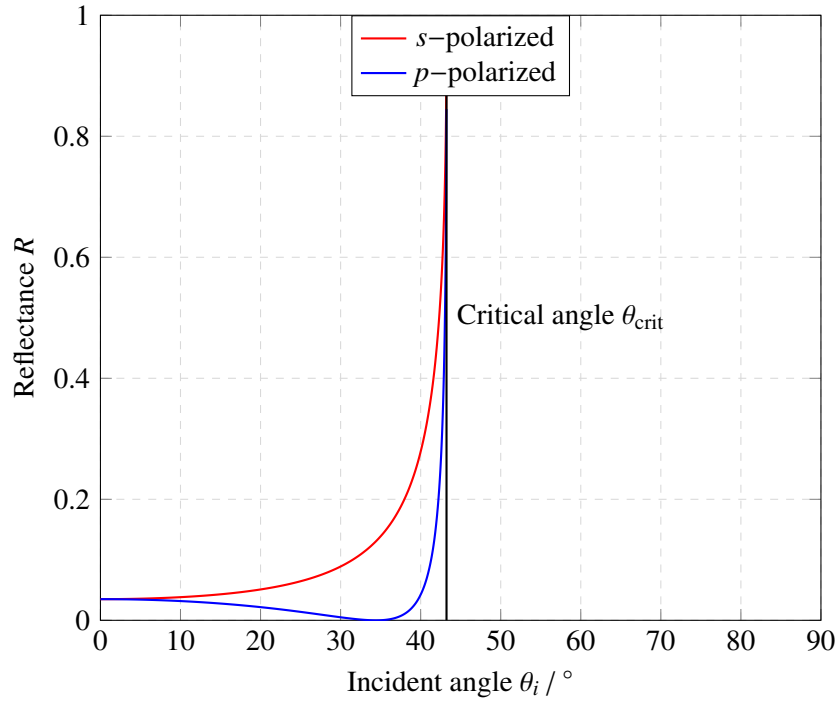


Figure 2.11: Reflectance of  $s$ - and  $p$ - polarized light at the boundary between fused silica and air, depending on the incident angle.

Fig. 2.11 depicts the case for the transition from fused silica into air, including the critical angle of total internal reflection  $\theta_{\text{crit}}$ . Total internal reflection leads also to a phase shift between the  $s$ - and  $p$ -polarized portion of the light. This shift, shown in Fig. 2.12, is given by

$$\delta = 2 \cdot \arctan \left( \frac{1}{\sin^2 \theta_i} \cdot \sqrt{(1 - \sin^2 \theta_i) \cdot \left( \sin^2 \theta_i - \left( \frac{n_2}{n_1} \right)^2 \right)} \right). \quad (2.49)$$

For the transition from UV-graded silica  $n_1 = 1.46$  into air  $n_2 \approx 1$ , a phase shift of  $\delta = 27.8^\circ$  follows. Since the photon polarization is desired to be at the maximum, these effects have to be kept in mind for proper beamline design.

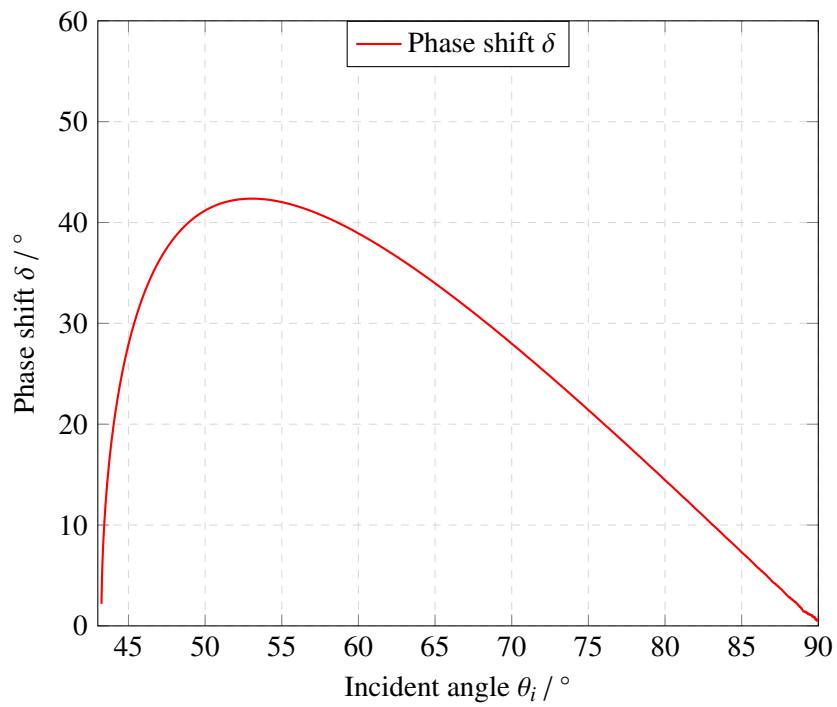


Figure 2.12: Phase shift between *s*- and *p*-polarized light depending on the incident angle for total internal reflection at the boundary between fused silica and air.

---

## The Compton Polarimeter at ELSA

---

### 3.1 A Brief History of the Compton Polarimeter at ELSA

The first iteration of the Compton polarimeter was installed by D.Doll in the course of his PhD thesis [2]. The photons were provided by an Ar<sup>+</sup>-Laser<sup>2</sup> positioned one floor above the accelerator plane, in the ground level of the Physics Institute. The laser beam was guided to the ELSA beam pipe using a system of six mirrors. Since the propagation distance was beyond 30 m, even small vibrations of the mirrors lead to issues concerning the beam pointing stability. In addition, the finite reflectivity of the used mirrors caused significant losses in intensity<sup>3</sup>. The resulting signal was difficult to distinguish from the background.

The next iteration in 2008[4] was to overcome these issues by installing a more powerful laser system much closer to the interaction region. This new laser system was designed to provide two beams with an intensity of 20 W each. The shorter distance to the interaction region, now being roughly 15 m instead of 50 m, was expected to improve the beam pointing stability in the interaction region. The beam shaping optics was redesigned to support both beams. To suppress beam losses, deflecting mirrors were interchanged with rectangular prisms whenever possible. A new station for the polarization measurement of the photon beam was installed. Enduring problems with the new laser system as well as hold-ups in finishing the detector system prevented the Compton polarimeter to begin operation.

After several necessary repairs have been performed on the laser system, a new attempt to commission the optical beamline was successfully made during the course of this thesis. After a new characterization of the laser system, the optical beamline was reevaluated and adjusted where necessary. Additional elements for measurement and diagnostic purposes were included into the beamline. With the detector system now being also operational, the setup of the Compton polarimeter is about to be completed to a great extend. Using the unpolarized electron beam and the self polarized electron beam, first measurements of the backscattered photons could be performed.

### 3.2 Setup of the Laser Beamline

#### 3.2.1 Optical Table

The optical table, displayed in Fig. 3.1 and 3.2, contains the laser system and beam shaping optics of the polarimeter, referring to Fig. 2.5 (a) and (b). It is set up in the transition area between the stretcher

---

<sup>2</sup> Coherent InnovaSabre 25 TSM

<sup>3</sup> Only 8 W of the emitted 13 W reached the interaction region.

ring and the experimental CB area in the Compton hatch. It consists of three levels, where the laser, optical elements and the detector can be placed [4]. The head of the MonoDisk Gemini laser system is positioned on the lower table. The supply unit, containing the pumping lasers as well as the chiller array, is set up in the experimental area. The supply- and control lines are connected to the laser head through a cable duct. The optical fibres are shielded with a separate pipe within the duct and a metal plating in the polarimeter area in order to prevent any mechanical damage. As for radiation protection, a concrete block is placed in line-of-sight between the laser head and the stretcher ring. Two remote controlled water cooled shutters<sup>1</sup> are attached to the laser head. The shutters are driven by compressed air and can be operated independently from one another. This allows for using one or both beams, depending on the measurement intended. The closing time is in the order of 300 ms [4]. After the shutter, the beam

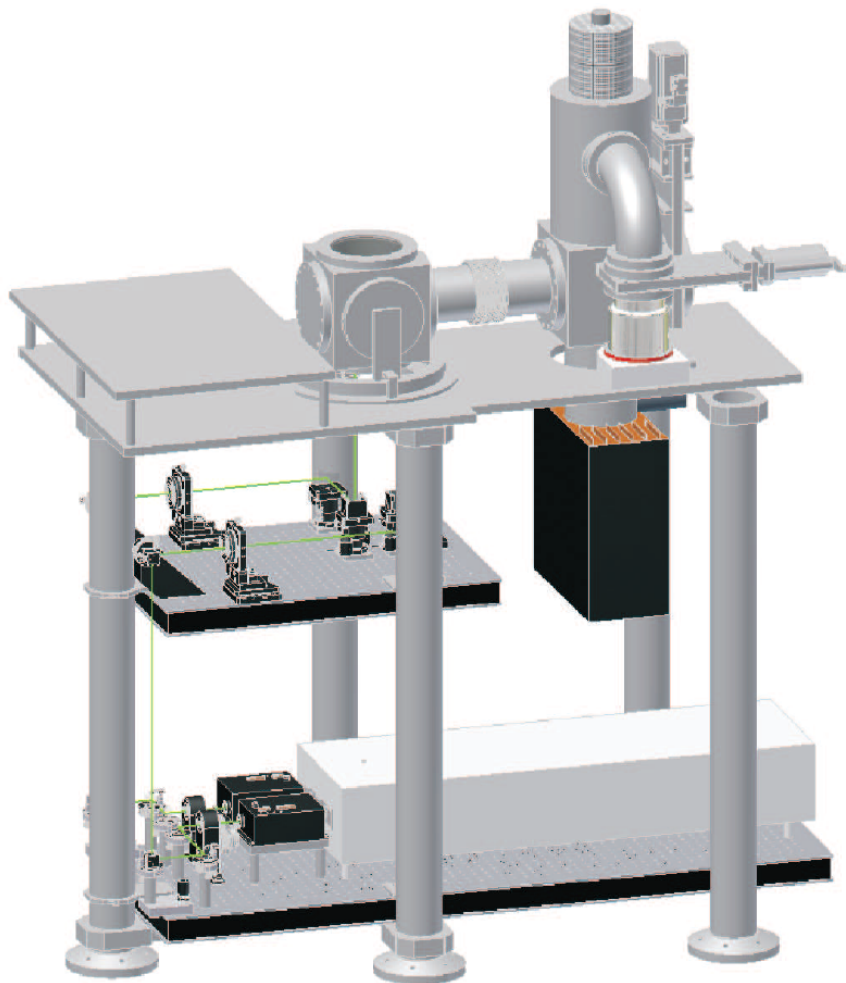


Figure 3.1: CAD model of the optical table. [4]

passes through a quarter-wave plate, which is placed in each beam path. These wave plates are fitted in pneumatically actuated mounts, allowing to switch positions between  $(+45 \pm 1)^\circ$  and  $(-45 \pm 1)^\circ$  in less than 250 ms, enabling a fast change in light polarization. Beam deflection is achieved by six rectangular prisms<sup>2</sup>. The first four prisms are each mounted on Cardan suspensions and can be adjusted

<sup>1</sup> SBS02 manufactured by AuRa Tech GmbH.

<sup>2</sup> UV-graded silica, AR-coated.

independently from one another. The last prism, responsible for coupling the beam into the vacuum beam pipe, can be adjusted electronically<sup>1</sup>. It can be operated on site or remote controlled as it is linked via ethernet to a PC. This remote control is implemented in the ELSA control system.

In order to maximize the photon density in the interaction region, both beam paths are equipped with focusing optics consisting of two lenses each. The first lens is fixed in place on the lower table. The second lens is mounted in an adjustable suspension on the upper table. Since the properties of both laser beams differ significantly, refer to section 3.3.2, different lens configurations have to be used. The first laser beam is focused by a succession of a biconvex and a biconcave lens, with focal lengths  $f_1 = -400$  mm and  $f_2 = 1300$  mm. The lenses in the second beam path are both biconvex with focal lengths  $f_1 = 300$  mm and  $f_2 = 1000$  mm. Every lens is manufactured with a diameter of 2". The lenses in the first beam path are AR-coated. For the second beam, only uncoated lenses were available for realization. These will be substituted by AR-coated lenses in the near future.



Figure 3.2: The optical table in its current state. The detector system is already in place on the rear end of the uppermost plate.

<sup>1</sup> Newport: NewStep™ Motion Control System.

For diagnostical purposes, the second beam can be splitted using a 50 : 50 beamsplitter and deflected into a water cooled powermeter<sup>1</sup>. This diagnostic branch in the beamline allows for precise monitoring of the laser power in beam 2.

In the first vertical chicane, both beamlines are equipped with a fast shutter<sup>2</sup> with a closing time of less than 15 ms. These shutters reflect the beam into a water-cooled copper beam dump. Since the first beam is widened significantly at this point, it has to be focused into the dump by a small lens with a focal length of  $f = 50$  mm to ensure complete beam dumping. The trigger signal for closing the shutters is provided by the detector system, both shutters are opened or closed at the same time.

In the coupling cube, the laser beams are coupled into the vacuum using a 2 inch fused silica mirror each. These mirrors are both 47.5 mm above and below the electron beam orbit respectively. Both mirrors are tilted by 3.1 mrad, allowing for crossing the beams in a distance of roughly 15 m in the interaction region within the QD25 magnet. Between both mirrors in the path of the backscattered photons there is a notch. Through this notch, the backscattered photons can pass unhindered. The rear end of the cube is made from thin aluminium in order to have as few material in the path of the backscattered photons as possible.

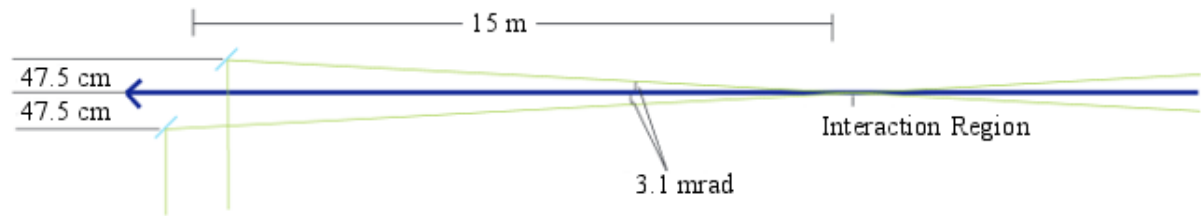


Figure 3.3: Sketch of the laser beams in the beamline. [4]

The vacuum system consists of three pump stages: a turbomolecular pump, an ion getter pump and a non-evaporable-getter pump. This setup allows for a high vacuum with pressures down to  $10^{-9}$  mbar. A pressure this low is necessary, since residual gas molecules may be taken up by the mirrors due to synchrotron radiation, leading to blackening of the coatings. The setup is followed by a DN150 valve, allowing to separate the system from the ELSA vacuum system.

### 3.2.2 Beamline

The Compton beamline leads across the transition area and through a core drilling in the radiation shielding into the ELSA tunnel. Inside the ELSA tunnel, a second vacuum pumping station is installed together with a beam monitor to survey the laser beam position inside the pipe. The beamline proceeds tangentially to the electron orbit in the center of the horizontally defocusing quadrupole magnet QD 25.

The interaction region, refer to Fig. 2.5 (c), of the Compton polarimeter consists of the section of the ELSA ring between the dipole magnets M24 and M25, with the QD25 magnet in the center. It has an overall length of roughly 1 m. The vertical electron beam divergence in a horizontally defocusing quadrupole has a minimum, the electron beam width  $\sigma_z$  has a maximum. Thus, the asymmetry in the backscattered photons' intensity profile is less disturbed. Since the electron beam travels in a straight line in an area of about 1 m around the quadrupole magnet, the signal-to-noise ratio obtained is higher compared to the dipole magnets.

<sup>1</sup> PowerMax USB - PM150-19C Power Sensor manufactured by Coherent Inc., specified to laser powers of up to 150 W.

<sup>2</sup> SmartShutter manufactured by Sutter Instruments.

The Compton beamline enters and leaves the electron beampipe through two ports with a diameter of 22 mm each, being the smallest passage in the beamline [4]. Before entering the dipole magnet M25, a second valve followed by a water-cooled copper plate is installed in the beamline. This copper plate is supposed to shield both valves from the synchrotron radiation. It can only be opened if both valves are opened as well.

After the laser has passed the dipole magnet M24, it leaves the vacuum through a saphir window with a diameter of 36 mm.



Figure 3.4: The Compton beamline in the ELSA tunnel. The optical beamline enters the electron beampipe in the M25 magnet and leaves the stretcher ring in the M24 magnet.

### 3.3 Measurements of the Laser System and Beamline

#### 3.3.1 Measurement Devices

##### The ModeMaster PC

One crucial device for the realization of this project was the *ModeMaster PC*. This device allows for a complete beam characterization in accordance to section 2.3. A sketch of the ModeMaster's layout can be seen in Fig. 3.5. The ModeMaster utilizes the principle of the four-cuts method presented in section

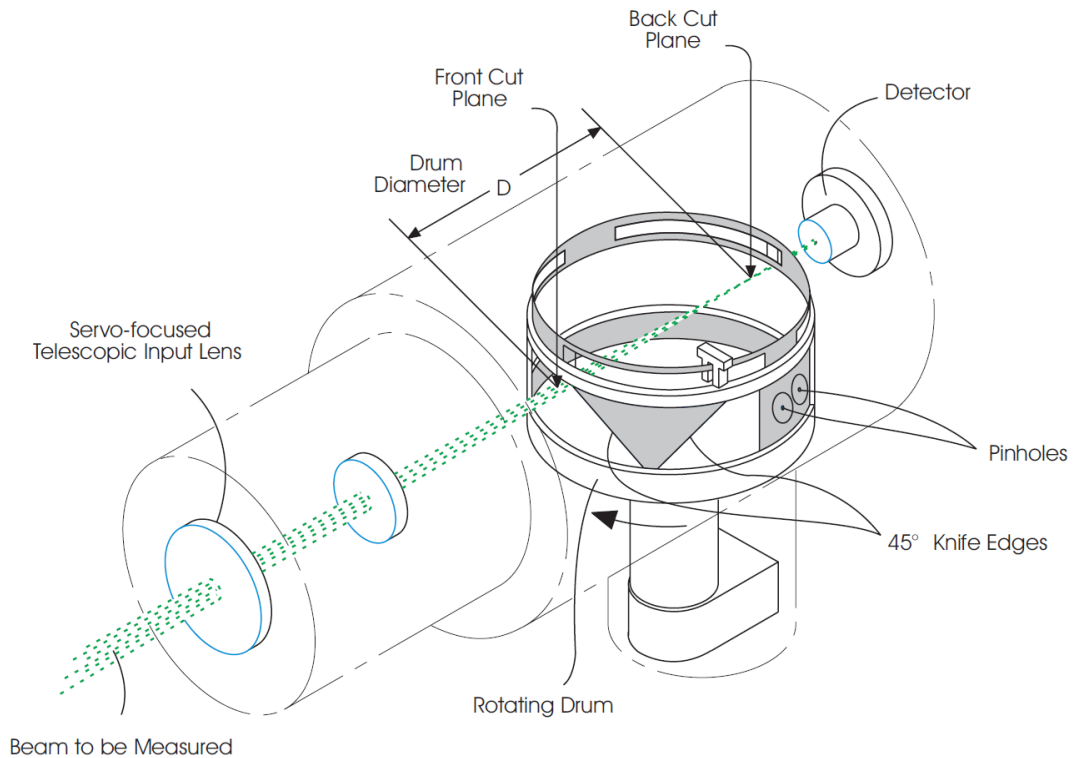


Figure 3.5: Sketch of the *ModeMaster PC* Beam Propagation Analyzer according to [17].

2.3.3. Its central components are the servo-focused input telescope system, the rotating drum and the detector. The four cuts method requires measuring the beam diameter at different positions as shown before. This is achieved using the servo-focused input lens. Instead of moving the detector, the incident beam is transformed by the input telescope. Moving the first lens effectively moves the beam relative to the stationary detector. The input lens is moved over a distance of 8 cm, during which the beam diameter is measured with 260 sampling points.

The beam diameter can be measured in two different ways. One possibility utilizes one of the two pinholes, diameter  $10\ \mu\text{m}$  and  $50\ \mu\text{m}$  each, in the rotating drum. This pinhole scans the incident beam intensity as shown in Fig. 3.6(a). Measuring the beam diameter this way of course can be troublesome, apart from requiring a radial symmetric beam. Since the pinholes are relatively small, deconvolution errors may occur. Another possibility makes use of two perpendicular knife edges in the rotating drum. These knives cut through the beam as the drum rotates with 10 Hz, resulting in an intensity profile as shown in 3.6(b) for both the horizontal and vertical plane, if the drum is tilted by  $45^\circ$ <sup>1</sup>. The intensity

<sup>1</sup> The software of the *ModeMaster PC* displays this azimuthal angle within the alignment screen with a precision of  $\pm 2^\circ$  [17].

profile can be described in terms of the Gauss error function. The pinhole scan is clipped at the  $\frac{1}{e^2}$  diameter definition of a Gaussian beam. In case of a knife-edge measurement, clipping the intensity profile at 84% and 16% gives a beam diameter equivalent to the  $\frac{1}{e^2}$  definition of a Gaussian beam. For any other set of clip levels, an appropriate width adjust factor has to be taken into account. Fig. 3.6(b) shows the principle for the different clip levels of 84% and 16% as well as 90% and 10%. Furthermore, the transverse beam position is determined by clipping the intensity profile at 50% incident intensity.

The knife edge measurement is not affected by deconvolution errors. Differing from the pinhole scans, a knife edge measurement utilizes the total beam intensity. Thus, the signal to noise ratio of the knife edge measurement is higher. For a given wavelength, a complete set of parameters describing the laser

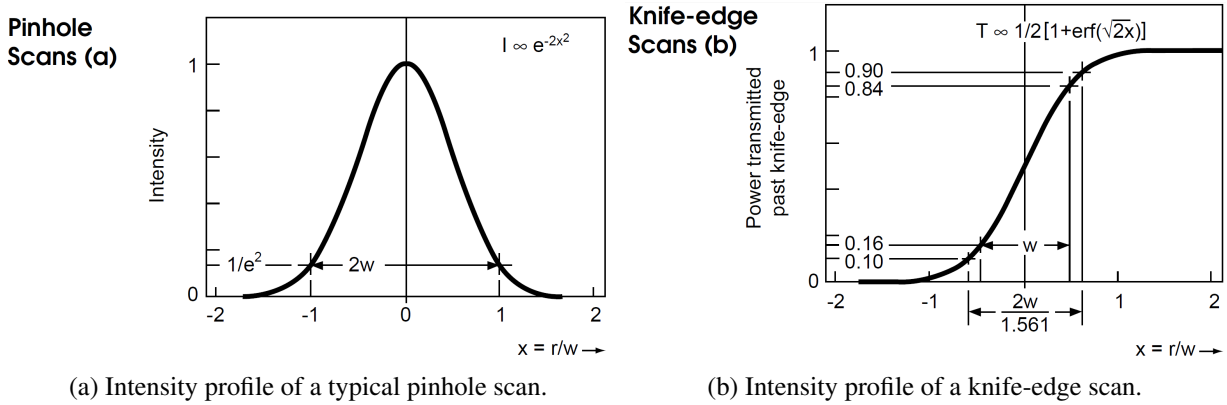


Figure 3.6: The intensity profiles used for both beam diameter measurement techniques as found in [17]. The  $x$ -axis is scaled with the beam width  $w$ . For the knife-edge measurement, the principle of different clip levels and width adjustment factors is shown.

beam is obtained. The measured parameters are shown in Table 3.1. In addition, the ModeMaster is able to measure the beam's angular and spatial displacement, enabling measurements of the transverse beam pointing stability, again for the horizontal  $X$  and vertical  $Y$  plane. For each beam measured, the so called *rad*-mode is given [12]. The *rad* or *R*-mode gives a radial symmetric approximation for the real beam measured.

Quantity	Symbol
Beam propagation factor	$M^2$
Beam waist diameter	$\omega_0$
Beam diameter at the input lens	$\omega_e$
Distance beam waist – ModeMaster	$z_0$
Rayleigh length	$z_R$
Full far-field divergence angle	$\theta$
Astigmatism	-
Focal asymmetry	-
Divergence asymmetry	-
Beam pointing stability	-

Table 3.1: The beam properties obtained by the *ModeMaster PC*.

It turned out that the ModeMaster detector saturates for incident beam powers  $P > 1$  W in contrary to the value of  $P > 2$  W given in the *ModeMaster PC* manual. For higher output powers, the ModeMaster

has to be modified in order to obtain consistent results. This is done by placing an aluminum disk with a small conical drilling<sup>1</sup> in front of the detector. This artificial aperture allowed measurements with higher laser intensities<sup>2</sup>. This was a custom solution, thus no specifications concerning the accuracy of the measurements could be given from the manufacturer. Consequently, measurements used for setting up and adjusting the beamline were performed with output powers  $P_{\text{out}} < 1$  W. The errors for the measured parameters are composed of the statistical errors as well as the systematic errors specified by [17].

### Intensity detectors

In this project, different types of intensity sensors were used. For small intensities, i.e. from a few nW up to 50 mW, a solid-state detector with a mirrored coating<sup>3</sup> was used. An incident light beam is reflected on the detector coating, the transmitted intensity is measured by the detector. According to the manufacturer, the calibration accuracy amounts to  $\pm 5.6\%$ .

For higher intensities, a different power sensor concept is used. This sensor type, called thermopile sensor, generates an output signal proportional to a local temperature gradient. The achievable temperature gradient without damaging the detector can be increased through air<sup>4</sup>- or water<sup>5</sup> cooling. The calibration accuracy of both sensors is given by  $\pm 2\%$ . All three sensors can sample their data with up to 10 Hz.

To observe effects on smaller time scales, measurements have been performed using a fast photo diode<sup>6</sup>, providing a time resolution of up to 1 ns.

### 3.3.2 The Complex Beam Parameter

In order to evaluate the optical beamline in terms of Gaussian optics, the complex beam parameter  $q(z)$  introduced in section 2.3 has to be measured. For both beams, this is done using the *ModeMaster PC*.

### Preliminary Measurements

In a first attempt to get familiar with the *ModeMaster PC* system, a new adjustment laser diode was characterized using the ModeMaster. The results obtained are shown in Table 3.2. The laser diode was operated with an output power  $P = 1.10 \pm 0.01$  mW, where the reading accuracy of the power sensor is considered.

Changing the distance from the ModeMaster to the adjustment laser diode should only influence the values of  $\omega_e$  and  $z_0$ . All other quantities should remain unchanged. During this first measurement, this behaviour could be verified with the ModeMaster.

The adjustment laser diode was also used to determine the focal lengths of the lenses used in the polarimeter. After measuring the beam parameter of the laser diode for a fixed distance  $d_{\text{MM-Laser}}$ , the lens in question was inserted in between. After a second beam parameter measurement, the focal length can be calculated using matrix optics according to 2.3.

---

<sup>1</sup>  $\varnothing = 0.75$  mm.

<sup>2</sup> The ModeMaster detector went into saturation for input powers exceeding 10 W.

<sup>3</sup> Coherent LM-2 VIS

<sup>4</sup> Coherent LM-45 HDT.  $P_{\text{max}} = 25$  W.

<sup>5</sup> Coherent PowerMax-USB PM150-19C.  $P_{\text{max}} = 150$  W.

<sup>6</sup> Thorlabs DET210 - High-speed silicon detector

	X	Y	R
$M^2$	$1.05 \pm 0.05$	$1.11 \pm 0.06$	$1.07 \pm 0.05$
$2\omega_0 / \text{mm}$	$1.54 \pm 0.03$	$1.57 \pm 0.03$	$1.56 \pm 0.03$
$2\omega_e / \text{mm}$	$1.62 \pm 0.18$	$1.65 \pm 0.18$	$1.64 \pm 0.18$
$z_0 / \text{m}$	$1.07 \pm 0.27$	$1.04 \pm 0.26$	$1.05 \pm 0.27$
$z_R / \text{m}$	$3.35 \pm 0.27$	$3.3 \pm 0.26$	$3.32 \pm 0.27$
$\theta / \text{mrad}$	$0.46 \pm 0.02$	$0.48 \pm 0.02$	$0.47 \pm 0.02$

	X	Y	R
$M^2$	$1.06 \pm 0.05$	$1.09 \pm 0.06$	$1.08 \pm 0.06$
$2\omega_0 / \text{mm}$	$1.56 \pm 0.03$	$1.58 \pm 0.03$	$1.57 \pm 0.03$
$2\omega_e / \text{mm}$	$1.56 \pm 0.18$	$1.58 \pm 0.18$	$1.57 \pm 0.18$
$z_0 / \text{m}$	$0.07 \pm 0.27$	$0.24 \pm 0.27$	$0.16 \pm 0.27$
$z_R / \text{m}$	$3.37 \pm 0.27$	$3.36 \pm 0.27$	$3.37 \pm 0.27$
$\theta / \text{mrad}$	$0.46 \pm 0.02$	$0.47 \pm 0.02$	$0.47 \pm 0.02$

Table 3.2: Beam parameter measurement with the adjustment laser diode. For the first measurement, the distance diode-ModeMaster was 0.76 m, for the second measurement 1.71 m. The results are given for both transverse planes as well as the *rad*-mode of the respective beam.

### The Laser Beam Parameter

The finally measured beam parameters for both beams of the MonoDisk laser system are shown in Table 3.3. The laser system was designed to have a beam propagation factor  $M^2 < 1.1$ . This beam quality is still provided for low beam intensities  $P < 0.5$  W. In terms of the beam waist and Rayleigh length, a significant asymmetry between both beams is evident.

For higher intensities however, the beam quality could not be maintained, as  $M^2$  increases for higher laser powers. As of now, this was only qualitatively reproducible, values for  $M^2 > 2$  have not been observed. The increase in  $M^2$  for higher laser powers was usually accompanied by an increase in the laser's intensity noise, as can be seen in Fig. 3.8, and thus in an increased inaccuracy of the four-cuts measurements performed by the ModeMaster, which requires a laser intensity noise  $< 2\%$  Peak-to-Peak. This laser noise was further investigated during the tests of the laser performance, refer to section 3.3.3.

### 3.3.3 Laser Performance Tests

#### First Measurements

The MonoDisk laser system was designed to provide an output power of  $2 \times 20$  W and was capable of doing so as of 2008 [4]. Following a series of repairs, amongst others the exchange of the SHG crystal and the laser disks, the laser performance needed to be reinvestigated. This was done by increasing the pumping diode current  $I_{\text{set}}$  by equidistant increments and, for each step, monitoring the output power of the laser system, the real diode current  $I_{\text{act}}$  as well as the diode voltage  $U_1$ . In the course of the repairs mentioned, the maximum adjustable diode current was increased from 40 A to 60 A in an attempt to maximize the achievable output power.

Two successive power ramps performed under similar conditions can be seen in Fig. 3.7. It is evident that the laser's behaviour is difficult to reproduce. In either case, a reproducible behaviour can be observed for pumping diode currents below 40 A. For higher pumping currents and therefore power densities incident on the laser disks, the laser's behaviour differs significantly. This can be caused e.g. by

Beam 1	X	Y	R
$M^2$	$1.03 \pm 0.06$	$1.04 \pm 0.06$	$1.07 \pm 0.06$
$2\omega_0 / \text{mm}$	$2.96 \pm 0.09$	$3.20 \pm 0.07$	$3.18 \pm 0.07$
$2\omega_e / \text{mm}$	$3.27 \pm 0.16$	$3.21 \pm 0.17$	$3.24 \pm 0.17$
$z_0 / \text{m}$	$-6.08 \pm 1.32$	$1.21 \pm 1.55$	$-2.68 \pm 1.48$
$z_R / \text{m}$	$12.97 \pm 1.23$	$15.02 \pm 1.35$	$14.43 \pm 1.27$
$\theta / \text{mrad}$	$0.23 \pm 0.01$	$0.21 \pm 0.01$	$0.22 \pm 0.01$
Beam 2	X	Y	R
$M^2$	$1.14 \pm 0.09$	$1.25 \pm 0.10$	$1.20 \pm 0.08$
$2\omega_0 / \text{mm}$	$0.27 \pm 0.01$	$0.29 \pm 0.01$	$0.28 \pm 0.01$
$2\omega_e / \text{mm}$	$5.35 \pm 0.17$	$5.43 \pm 0.15$	$5.39 \pm 0.14$
$z_0 / \text{m}$	$-1.95 \pm 0.15$	$-1.94 \pm 0.15$	$-1.95 \pm 0.15$
$z_R / \text{m}$	$0.99 \pm 0.01$	$0.10 \pm 0.01$	$0.10 \pm 0.01$
$\theta / \text{mrad}$	$2.74 \pm 0.17$	$2.79 \pm 0.15$	$2.77 \pm 0.15$

Table 3.3: Beam parameter measurement for both laser beams. The distance between the ModeMaster and the Laser was 1 m.

undesired thermal effects inside the resonator.

After reaching the maximum diode current, the time dependence of the output power was monitored. The results are shown in Fig. 3.8. As can be seen, the output power is not equally distributed between both beams. One possible reason is the orientation of the SHG crystal, which has a significant impact on the frequency-doubled beam's intensity due to the phase-matching conditions, refer to section 2.2.2.

Of further notice is the peak in the output power at the time the maximum pumping current is reached. The output power then decreases significantly, while the measured power fluctuations increase in amplitude. Within the flat-top, the output power varied by  $\Delta P \approx 2 \text{ W}$ . The reason behind this behaviour is not completely understood. Later studies of the pumping diodes showed, however, that the reason is most likely located in the laser's resonator.

The flat-top was usually reached after 45 min, the total output power usually varied between  $20 \text{ W} \leq P_{\text{tot}} \leq 30 \text{ W}$ , which is significantly less than the design total output power of 40 W. The decrease in output power is most likely a consequence of the different necessary attempts made to increase the laser's long-term stability.

The temperature dependence of the laser performance was studied using a portable air conditioning system. The air conditioner provided an environment temperature of  $17^\circ \text{C}$  around the laser casing. The pumping diodes were ramped up to their maximum allowed current while the output power of the laser system was monitored. After roughly 2 h, the air conditioning was used to heat the laser's environment. As can be seen in Fig. 3.9, the temperature increased by a few degrees in the following.

This increase in temperature was linked with a decrease in the laser's output power. For a temperature difference of  $6^\circ \text{C}$ , the total output power decreased by about 3 W. Despite these promising results, due to the cost-benefit-ratio, no additional laser cooling system could be implemented in the course of this work.

The laser's performance proved to be even more sensitive to the built in possibility of changing the temperature of the water used for cooling the laser disks. The chillers responsible for this temperature control allow the water temperature to be chosen between  $18^\circ \leq T \leq 25^\circ \text{C}$ . Temperatures higher than  $25^\circ \text{C}$  cause a shutdown of the laser<sup>1</sup>. Within this temperature range, the laser's output power varied by a factor  $\leq 2$ . For a water temperature  $T = 18^\circ \text{C}$ , the laser output power reached its maximum.

<sup>1</sup> The laser interlock does not allow temperatures that high in order to protect the laser disks from thermal damage.

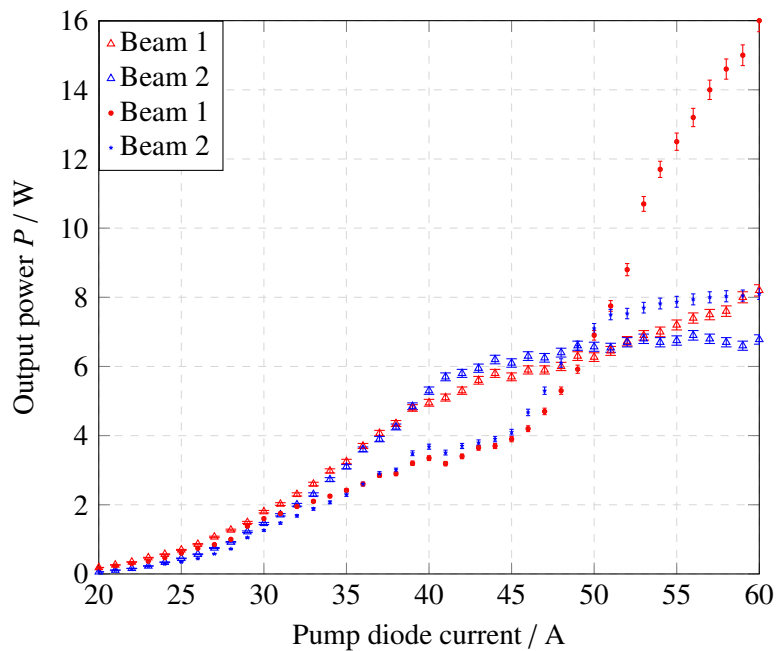


Figure 3.7: Output power of both laser beams depending on the pumping diode current for two successive ramps.

### Power Stability

To further investigate the power instability and decrease in beam quality at higher output powers, the time dependent beam intensity was monitored using a fast silicon detector. In order to study the beam fluctuations at the maximum pumping diode current, the beam was deflected into a beamdump using a dielectric mirror. The intensity transmitted through the mirror was focused onto the diode using a lens with a focal length  $f = 50$  mm. For incident laser powers  $P_{in} \approx 15$  W, the transmitted intensity was in the order of 3 mW, protecting the diode from damage. The photo diode's signal was read out using an oscilloscope.

The resulting transmitted incident intensity was comparable to the operating power of the adjustment laser diode as well as a pulsed laser pointer. In Fig. 3.10 the results for the disk laser as well as the adjustment laser are shown. Compared with the adjustment diode, the MonoDisk signal shows greater fluctuations in intensity. These fluctuations could result from various sources:

- Mechanical concussions during operation in the laser laboratory.
- Variations in the pumping power resulting from any noise in the power supply unit.
- Unwanted laser dynamics inside the resonator.

An external mechanical source could quickly be ruled out, since this would also have influenced the measurements with the adjustment diode.

The next step was to study the behaviour of the two pumping diodes, by guiding them onto a power sensor using an additional optical fibre<sup>1</sup>. The output power of the pump diodes was expected to be in the order of 100 W. Only one power sensor available was able to measure intensities of that magnitude. Thus, the respective second pumping diode was left connected to the disk laser. The pumping diodes showed a

<sup>1</sup> Kindly provided by Jan Gettkant, Dausinger+Giesen GmbH.

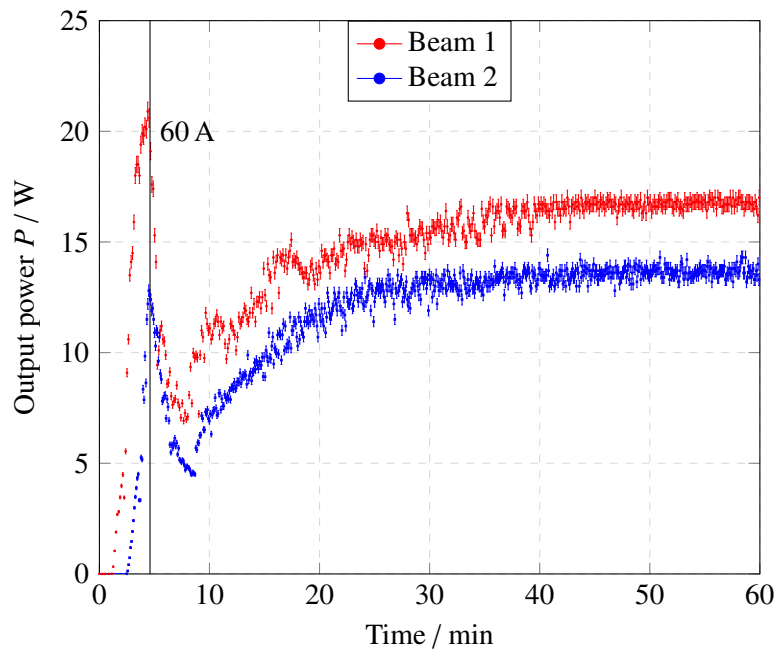


Figure 3.8: Laser output power in dependence of the time passed. After about 5 min, the maximum pumping current  $I_{\text{Set}} = 60 \text{ A}$  was reached.

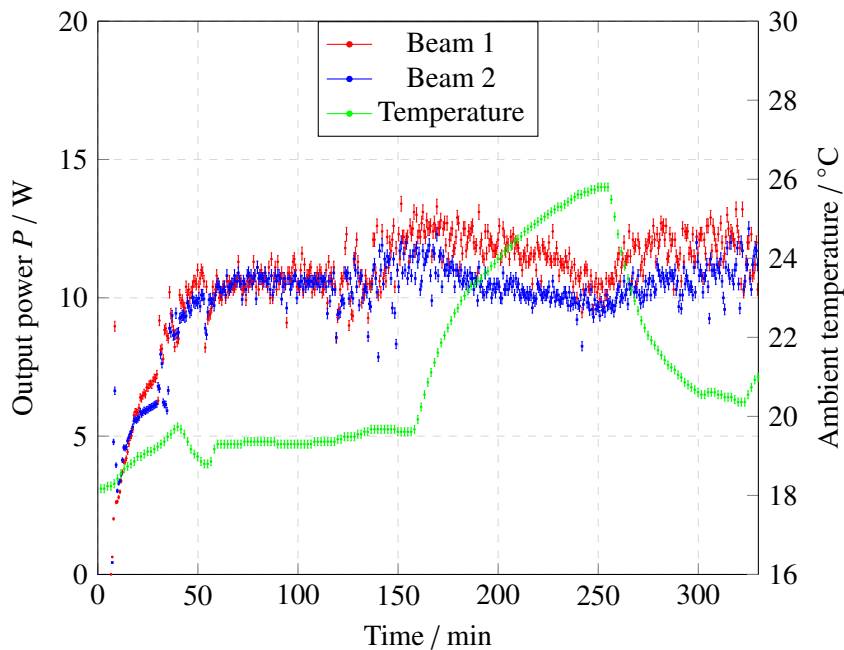


Figure 3.9: Output power in dependence of temperature changes measured on the laser's casing.

linear behaviour in response to a current increase as is shown in Fig. 3.11. The second pumping diode provides a little less output power. Both diode lasers did not show any significant power fluctuation, as

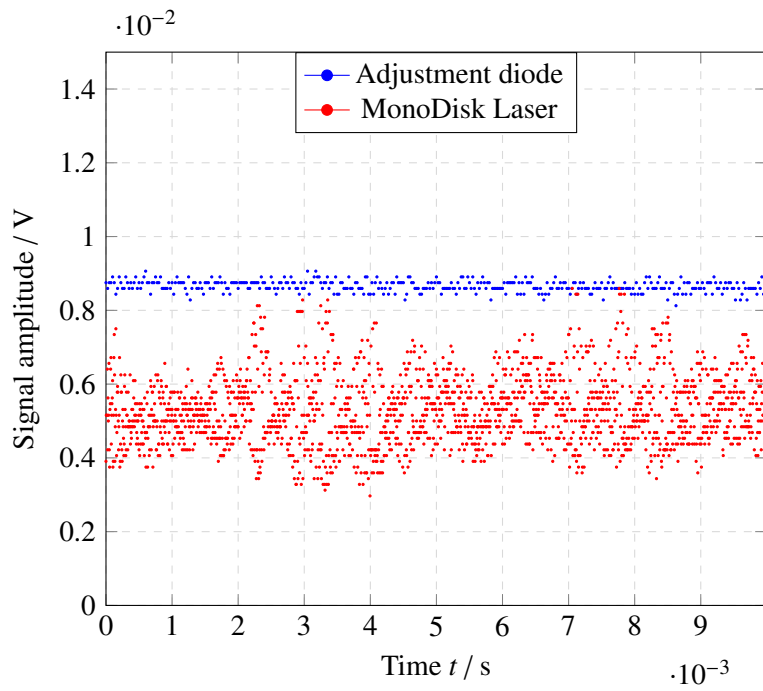


Figure 3.10: Photo diode response to the adjustment laser diode and the MonoDisk laser.

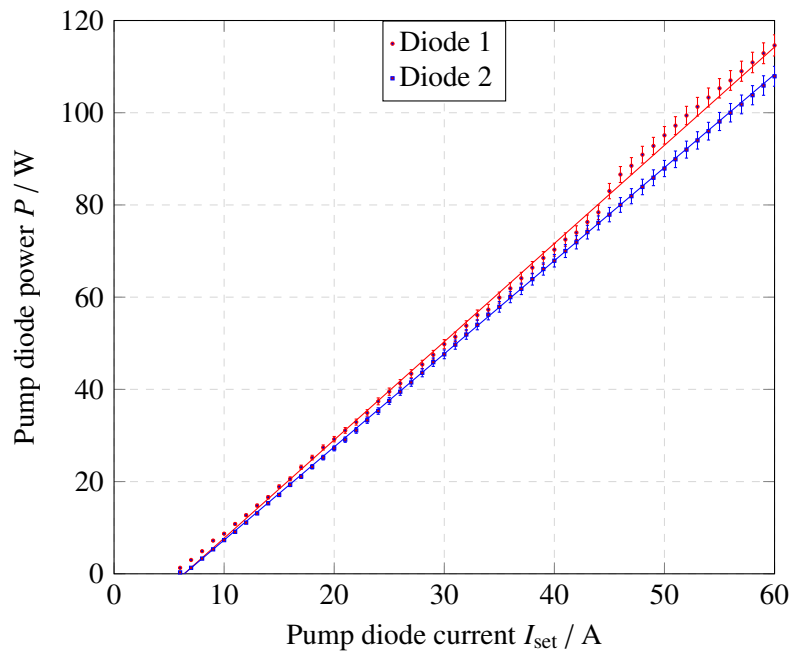


Figure 3.11: Pump diode power in dependence of the pumping current.

can be seen in Fig. 3.12.

The laser's intensity noise can therefore be assumed to be caused by laser dynamics inside the resonator.

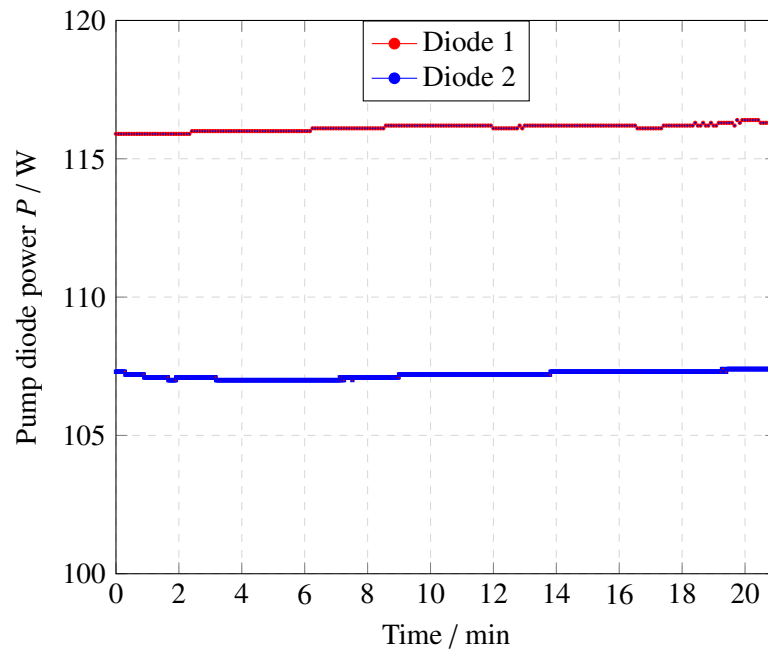
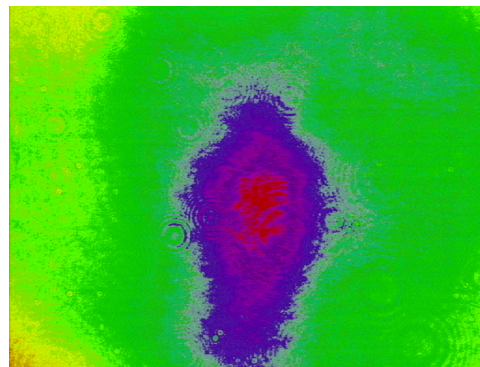


Figure 3.12: Pump diode power in dependence of the passed time for a pumping current  $I_{\text{Set}} = 60$  A.

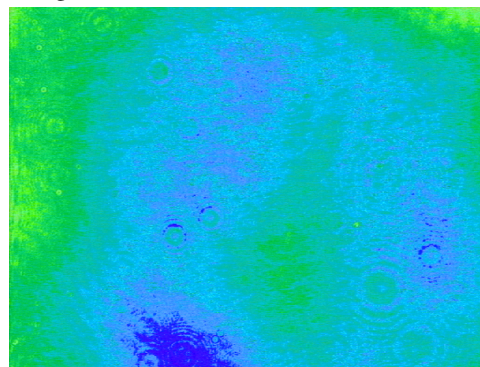
One possible process is the so called *mode hopping*, i.e. the varying power distribution over the modes excited in the laser resonator. An increasing portion of higher order modes would also lead to an increased  $M^2$  of the laser beam. This behaviour could be resolved using a CCD<sup>1</sup>-camera placed in the beamline.<sup>2</sup> In Fig. 3.13, such a mode hop is shown. In this case, the two dominant modes were the fundamental Gaussian mode  $\text{TEM}_{00}$  and the  $\text{TEM}_{01^*}$ , also known as the *doughnut* mode. The  $\text{TEM}_{01^*}$ -mode is a superposition of the  $\text{TEM}_{00}$ - and the  $\text{TEM}_{01}$ - mode.

<sup>1</sup> Charge-coupled device

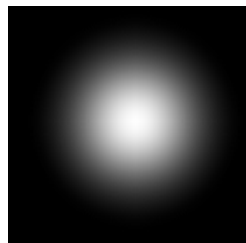
<sup>2</sup> Kindly provided by M. Switka.



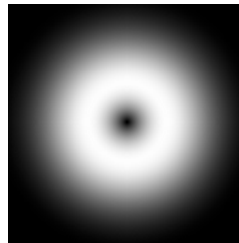
(a) Asymmetric beam with the dominant mode being the  $TEM_{00}$ -mode.



(b) Beam with the dominant mode being the  $TEM_{01^+}$ -mode.



(c) Sketched fundamental  $TEM_{00}$ -mode.



(d) Sketched  $TEM_{01^+}$ -mode.

Figure 3.13: Mode hops resolved using a CCD camera. The dominant mode of the laser beam switches from the  $TEM_{00}$ -mode to the  $TEM_{01^+}$ -mode.<sup>1</sup>

### The Laser's Degree of Polarization

The time needed for an electron beam polarization measurement with a reasonable accuracy is inversely proportional to the degree of circular polarization. Therefore, a high degree of circular polarization is required.

The setup used in the beamline uses quarter-wave plates in order to obtain the needed circularly polarized photon beam. The degree of circular polarization achievable is therefore directly dependent on the initial degree of linear polarization provided by the laser system. If not sufficient, a polarization filter

<sup>1</sup> Courtesy of M. Switka.

would have to be placed in front of the quarter-wave plates. This would lead to a significant intensity loss of up to 50 % for an unpolarized laser beam and is thus not desired. Therefore, the degree of polarization of the laser beams is measured.

In order to do so, the laser beam was split with a polarizing beam splitter. The intensity in each branch following the splitter was measured. A sketch of the setup is shown in Fig. 3.14.

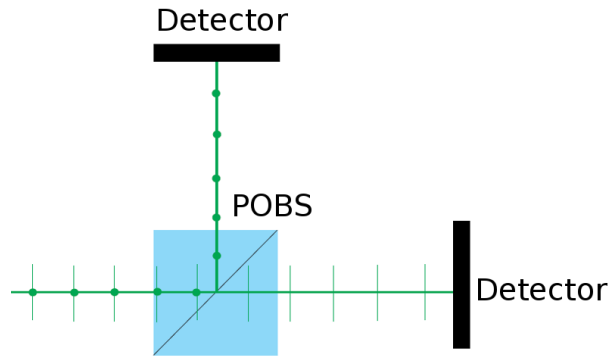


Figure 3.14: Sketch of the setup used to determine the degree of linear photon polarization provided by the MonoDisk laser system.

According to section 2.1.2, the degree of linear polarization  $P_\gamma$  is given by  $P_\gamma = \frac{I_{pol}}{I_{tot}}$ . The intensity of the  $s$ -polarized light was measured in dependence of the total output power. Fig. 3.15 shows the results for output powers up to 2 W. For any output power provided by the laser system, the degree of linear polarization remained constant within the accuracy of measurement and is listed in Table 3.4. The measured degree of polarization is still sufficient and within the specifications given by the manufacturer. An additional polarization filter is not necessary.

	Beam 1	Beam 2
$P_\gamma / \%$	$99,97 \pm 0,01$	$99,95 \pm 0,05$

Table 3.4: Degree of linear polarization in  $s$ -direction of the ELS MonoDisk laser beams.

### 3.3.4 The Focusing Optics

The maximum photon density possible in the interaction region is desired. In order to achieve this, the following goals were set:

- The focal point of the telescope has to be in the center of the QD25 quadrupole magnet, around 16 m distant from the laser head.
- The photon beam waists in the focal point should be less than 1 mm.
- The interaction region covers a distance of about 1 m. As a compromise to ensure high photon densities within this area, the Rayleigh lengths of either photon beam should not be smaller than 0.5 m.
- The photon beam diameter must not exceed the limitations given by the beamline aperture. The bottlenecks worth mentioning are the first four prisms with a surface area of  $25 \times 25 \text{ mm}^2$  and the ports in the beamline with a diameter of 22 mm.

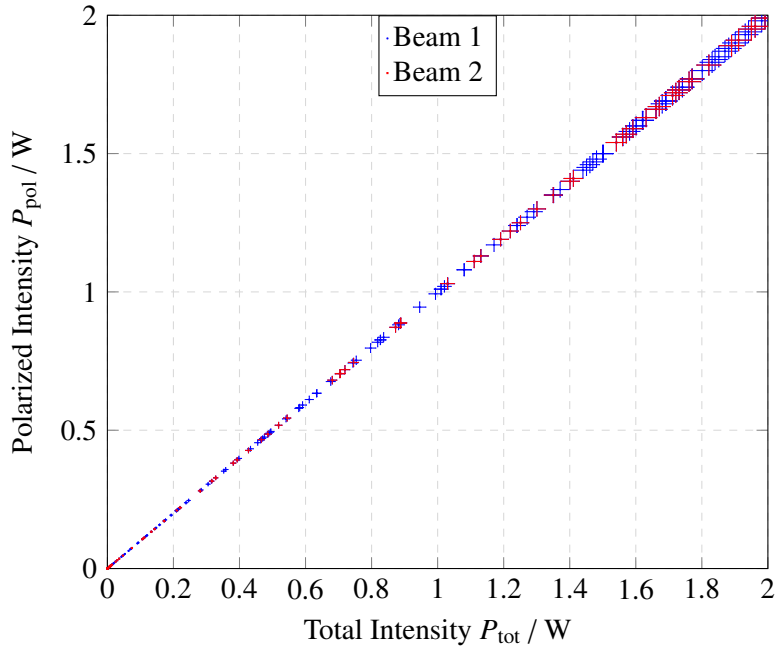


Figure 3.15: Linearly polarized intensity in dependence of the total incident intensity. The degree of polarization is given by the ratio of both values.

The necessary calculations have been performed using the software Mathematica [18].

The first step in determining a suitable lens system, consisting of two lenses with focal lengths  $f_1, f_2$  and a distance  $d$  between them, was measuring the initial beam parameter  $q_0$  of each beam as described in section 3.3.2. Using the optical matrix in dependence of  $f_1, f_2$  and  $d$ , a set of telescope setups fulfilling the conditions above has been calculated using equation 2.34. Initially, there could be an infinite amount of solutions. By arbitrarily defining the position of the first lens and only allowing for discrete values of  $f_1, f_2$  and  $d$  within a specified range, a finite set could be determined. Since lenses are usually available with discrete focal lengths and the distance between two lenses can only be determined with a finite accuracy, this approach was considered justified. The beam waist  $\omega_0$  and the Rayleigh length  $z_R$  were calculated for each set of values and filtered using the above conditions, giving a first approach to a final setup. This process is quite time- and resource-consuming and does not always yield a suitable solution, depending on the restrictions for  $f_1, f_2$  and  $d$ .

A more effective approach prioritized the different lenses already available for this project. The matrix  $M_{\text{tot}}(d)$  was calculated for different combinations of those lenses. Some results for both beams are shown in Table 3.5. The positions of the first lens are chosen as  $z_0 = 0.455$  m for Beam 1 and  $z_0 = 0.655$  m for Beam 2 respectively.

A combination of  $f_1 = -400$  mm and  $f_2 = 1300$  mm was chosen first, since AR-coated lenses with these focal lengths and appropriate suspensions were already available. For Beam 1, sufficient results could be achieved. For Beam 2, this telescope had to be redesigned. Since Beam 2 has a higher divergence, using a defocusing lens leads to a beam width easily exceeding the limitations given by the beamline. Instead, a combination of two focusing lenses,  $f_1 = 300$  mm and  $f_2 = 1000$  mm, was used. These lenses were originally intended for the use in synchrotron light diagnosis and manufactured with a diameter of 2 inch, thus fitting in the suspensions in use. Unfortunately, both lenses are not AR-coated.

Beam 1					Beam 2				
$f_1$ / mm	$f_2$ / mm	$d$ / m	$z_R$ / m	$\omega_0$ / mm	$f_1$ / mm	$f_2$ / mm	$d$ / m	$z_R$ / m	$\omega_0$ / mm
300	1300	1.732	0.601	0.325	-400	1300	1.108	0.497	0.312
-75	300	0.231	1.001	0.419	-300	1000	0.820	0.572	0.335
300	1000	1.374	1.138	0.447	300	1300	1.805	0.606	0.345
-400	1300	1.026	1.182	0.455	-500	1300	1.047	0.710	0.374
-300	1000	0.771	1.217	0.462	300	1000	1.445	1.149	0.475
-100	300	0.206	1.791	0.560	-750	1300	0.917	1.303	0.507
100	300	0.406	1.792	0.561	100	300	0.413	1.329	0.511

Table 3.5: Possible combinations of lenses fulfilling the desired conditions, sorted by the waist size in the interaction region. The telescopes currently used are highlighted.

### 3.3.5 Measurements of the Adjusted Beam

#### Beam Parameter in the Interaction Region

The telescopes determined through the described method were implemented and adjusted. The ModeMaster was placed after the interaction region at the end of the vacuum part of the beamline to measure the complex beam parameter in the interaction region,  $q_{IP}$ . The telescopes were fine-tuned until the beam waist was located inside the QD25 magnet within the accuracy of the measurement. The final beam parameter was measured at two locations behind the interaction region. The distances ModeMaster to QD25 were  $d_1 = 3.658$  m and  $d_2 = 3.788$  m each. A greater distance between both points could not be realized due to spatial restrictions. Since the accuracy of the beam waist location scales with the Rayleigh length, a finer sampling would be expedient. Within the accuracy of measurement, both beams have their beam waist within the QD25 magnet. The results are consistent with the expectations given by Table 3.5 in terms of waist size  $\omega_0$  and Rayleigh length  $z_R$  and are presented in Table 3.6. The deviations from the calculated results for Beam 2 are due to a slightly different lens positioning as well as a higher value for  $M^2$ , leading to a higher divergence of the beam.

Fig. 3.16 shows the laser beam widths and the electron beam widths  $\sigma_x$  and  $\sigma_z$  for an electron beam energy of 3.2 GeV. These beam widths are obtained using the simulated energy-dependant emittance  $\epsilon$  and the TWISS parameters of ELSA. The horizontal beam emittance for an electron energy of 3.2 GeV was obtained from the simulated ELSA model in the control system to be  $\epsilon_x = 9.057 \cdot 10^{-7}$  m rad. The TWISS parameters are provided by an ELEGANT model of the stretcher ring. The vertical emittance was assumed to be  $\epsilon_z = 0.1\epsilon_x$ . Inside a horizontally defocusing quadrupole magnet, the horizontal and vertical electron beam widths are almost the same.

Since the electron beam size is smaller for lower electron energies, a similar plot for an electron beam energy of 1.7 GeV is also shown in Fig. 3.17.

For electron energies in the order of 3.2 GeV, the photon beam width is significantly smaller than the electron beam widths for all values of  $M^2$  observed. For electron energies in the order of 1.7 GeV, this can only be assumed for  $M^2 \lesssim 1.6$ .

#### Degree of Circular Polarization in the Interaction Region

The degree of circular polarization of both beams was measured right behind the vacuum part of the beamline, roughly 3.6 m distant from the QD25 magnet.

At first, the quarter-wave plates in the pneumatic suspensions had to be set up appropriately. This was

	Beam 1		Beam 2	
	$d_1$	$d_2$	$d_1$	$d_2$
$M_X^2$	$1.05 \pm 0.08$	$1.07 \pm 0.08$	$1.25 \pm 0.08$	$1.43 \pm 0.07$
$M_Y^2$	$1.06 \pm 0.08$	$1.06 \pm 0.08$	$1.33 \pm 0.08$	$1.52 \pm 0.08$
$M_R^2$	$1.09 \pm 0.08$	$1.09 \pm 0.08$	$1.59 \pm 0.09$	$1.53 \pm 0.08$
$2\omega_{0,X}/\text{mm}$	$1.03 \pm 0.04$	$1.02 \pm 0.05$	$0.62 \pm 0.02$	$0.70 \pm 0.01$
$2\omega_{0,Y}/\text{mm}$	$1.16 \pm 0.04$	$1.13 \pm 0.04$	$1.09 \pm 0.03$	$0.92 \pm 0.02$
$2\omega_{0,R}/\text{mm}$	$1.13 \pm 0.04$	$1.15 \pm 0.03$	$0.96 \pm 0.03$	$0.82 \pm 0.02$
$2\omega_{e,X}/\text{mm}$	$2.75 \pm 0.08$	$2.86 \pm 0.07$	$5.17 \pm 0.06$	$5.34 \pm 0.05$
$2\omega_{e,Y}/\text{mm}$	$2.15 \pm 0.09$	$2.23 \pm 0.07$	$2.75 \pm 0.09$	$4.22 \pm 0.06$
$2\omega_{e,R}/\text{mm}$	$2.47 \pm 0.08$	$2.56 \pm 0.07$	$4.14 \pm 0.07$	$4.81 \pm 0.05$
$z_{0,X}/\text{m}$	$-3.83 \pm 0.35$	$-3.97 \pm 0.36$	$-3.86 \pm 0.34$	$-3.96 \pm 0.32$
$z_{0,Y}/\text{m}$	$-3.02 \pm 0.29$	$-3.14 \pm 0.29$	$-3.17 \pm 0.28$	$-3.81 \pm 0.30$
$z_{0,R}/\text{m}$	$-3.47 \pm 0.32$	$-3.59 \pm 0.32$	$-3.68 \pm 0.33$	$-3.90 \pm 0.31$
$z_{R,X}/\text{m}$	$1.54 \pm 0.18$	$1.52 \pm 0.15$	$0.47 \pm 0.05$	$0.53 \pm 0.04$
$z_{R,Y}/\text{m}$	$1.94 \pm 0.20$	$1.85 \pm 0.16$	$1.38 \pm 0.14$	$0.85 \pm 0.07$
$z_{R,R}/\text{m}$	$1.78 \pm 0.18$	$1.73 \pm 0.16$	$0.87 \pm 0.09$	$0.68 \pm 0.05$
$\theta_X/\text{mrad}$	$0.67 \pm 0.04$	$0.67 \pm 0.04$	$1.33 \pm 0.05$	$1.34 \pm 0.07$
$\theta_Y/\text{mrad}$	$0.6 \pm 0.04$	$0.61 \pm 0.04$	$0.8 \pm 0.05$	$1.08 \pm 0.05$
$\theta_R/\text{mrad}$	$0.63 \pm 0.04$	$0.64 \pm 0.04$	$1.1 \pm 0.06$	$1.32 \pm 0.06$
Astigmatism/%	$45.5 \pm 4.60$	$48.2 \pm 4.11$	$79.3 \pm 5.65$	$22.2 \pm 1.11$
Waist Asymmetry	$1.13 \pm 0.08$	$1.11 \pm 0.08$	$1.77 \pm 0.13$	$1.32 \pm 0.07$
Divergence Asymmetry	$0.9 \pm 0.06$	$0.91 \pm 0.05$	$0.60 \pm 0.03$	$0.81 \pm 0.04$

Table 3.6: Measured properties of the adjusted MonoDisk laser beams. The distance between the ModeMaster and the interaction region is given by  $d_1 = 3.658$  m and  $d_2 = 3.788$  m. The results are given for both transverse planes as well as the *rad*-mode.

done by placing the wave plate in the beam path, followed by a polarizing beamsplitter. At angles  $\pm 45^\circ$  of the fast axis, the intensities in both branches following the beamsplitter should be equal. At  $0^\circ$ , the *p*-polarized branch should be minimal. Both stopping points are set accordingly, so the quarter-wave plate can be switched between  $\pm 45^\circ$ .

A second quarter-wave plate and polarizing beamsplitter is then used at the point of interest to determine the degree of polarization. A sketch of the setup can be seen in Fig. 3.18. The principle of measurement is also applied in the polarization measurement station: The circularly polarized photon beam passes through the second quarter-wave plate. For an orientation  $\pm 45^\circ$  of the second wave plate, the resulting beam is linearly polarized. For any other orientation, an elliptical polarization is expected. If one measures the intensity in one of the branches following the beamsplitter, a sinusoidal dependency of the angle of the fast axis is expected.

This measurement is performed twice, for both orientations  $\pm 45^\circ$  of the first wave plate. The results for both beams are shown in Figs. 3.19 and 3.20. The degree of circular polarization is obtained by

$$P_\gamma = \frac{\sqrt{S_3^2}}{S_0}. \quad (3.1)$$

$S_3$  is given by the transmission in the respective branch of the polarizing beamsplitter. The degree of

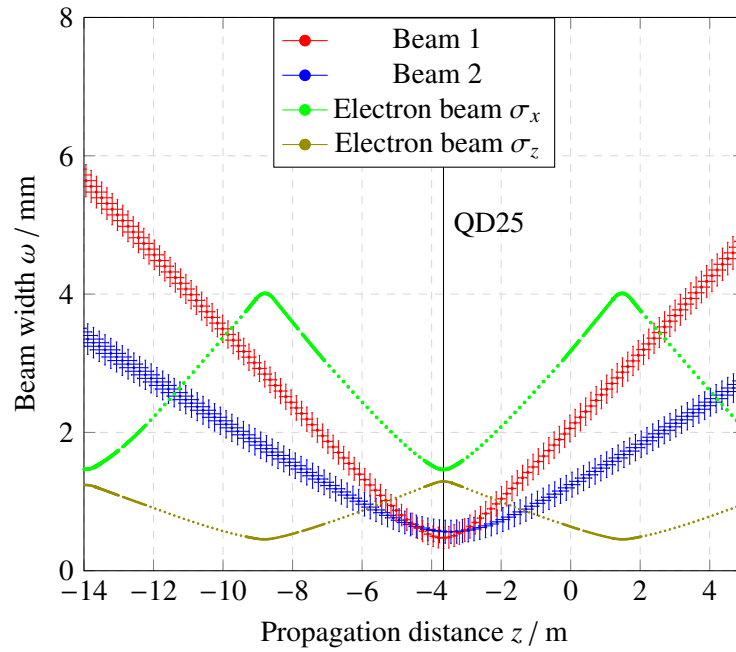


Figure 3.16: Adjusted beam propagation in the vacuum beam line for an electron beam energy of 3.2 GeV. The ModeMaster was placed at  $z = 0$ .

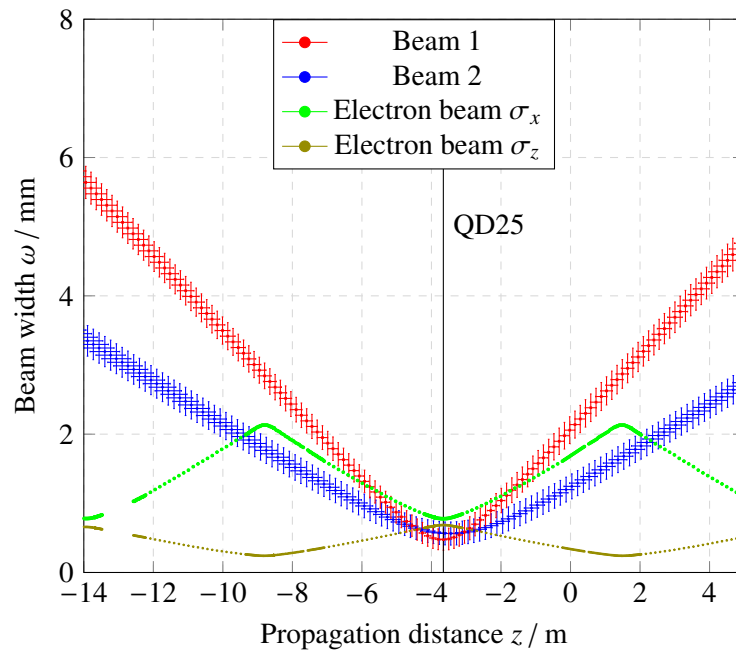


Figure 3.17: Adjusted beam propagation in the vacuum beam line for an electron beam energy of 1.7 GeV. The ModeMaster was placed at  $z = 0$ .

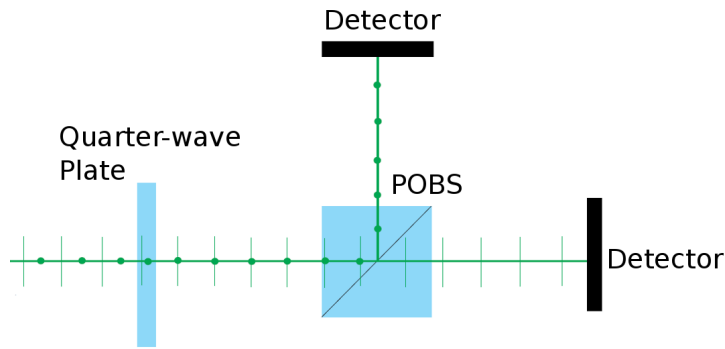


Figure 3.18: Sketch of the setup used to measure the photon beam's degree of circular polarization.

polarization shown in Table 3.7 is determined at an angle  $45^\circ$  of the second wave plate's fast axis. Due to misalignment of the plate within the suspension, this corresponds to an absolute angle  $41^\circ$  read off from the scale. Within the accuracy of measurement, an asymmetry is visible for both beams. This is

	$\pm 45^\circ$	Beam 1	Beam 2
$P_\gamma / \%$	$-45^\circ$	$99.95 \pm 0.07$	$97.99 \pm 0.06$
$P_\gamma / \%$	$+45^\circ$	$99.51 \pm 0.06$	$95.42 \pm 0.06$

Table 3.7: Degree of circular polarization of the MonoDisk laser beams obtained in the vacuum beamline.

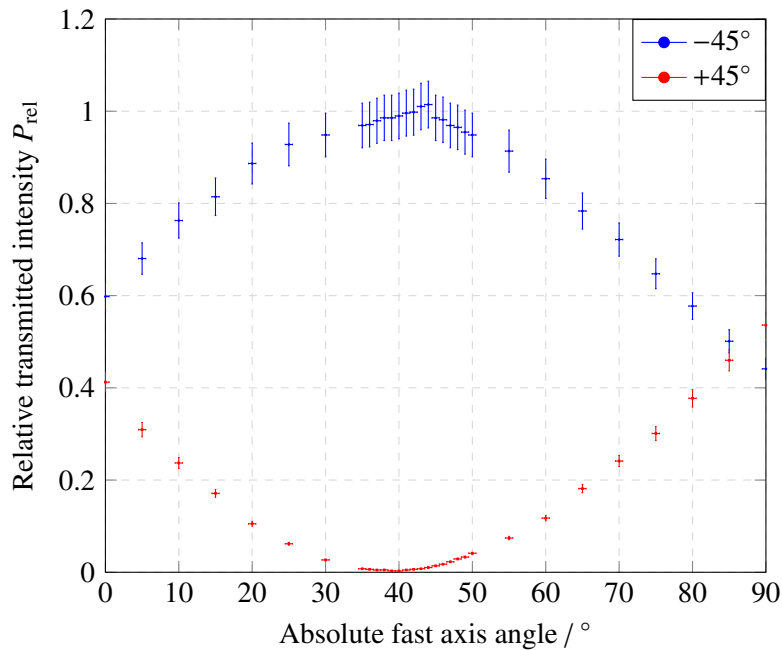


Figure 3.19: Measurement of the circular degree of polarization of Beam 1.

most likely caused by the first quarter-wave plate. This wave plate is mounted in a pneumatic suspension designed to endure many switching processes. The suspension's scale can only be aligned with the wave

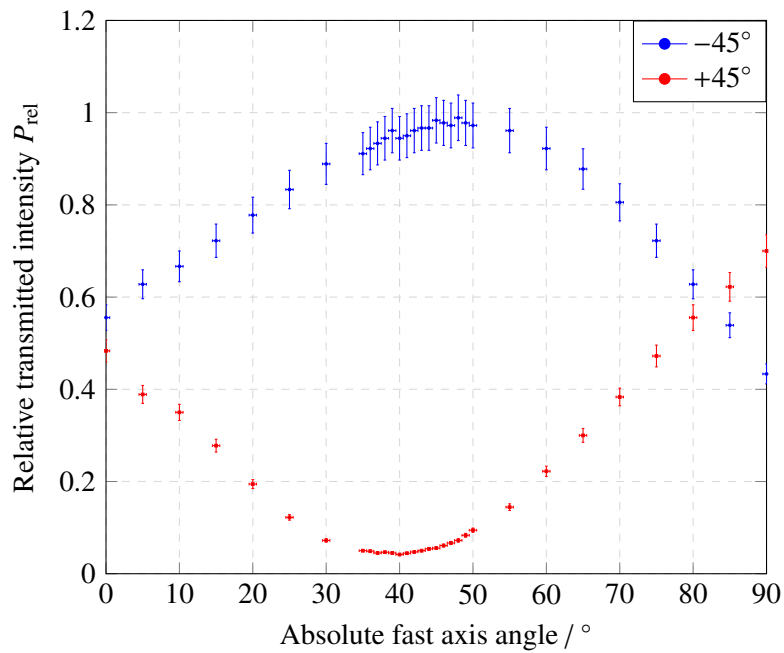


Figure 3.20: Measurement of the circular degree of polarization of Beam 2.

plate's fast axis with an accuracy of about  $2^\circ$ . When fixating the stopping points of the pneumatic switch, an additional misalignment usually occurs.

The degree of polarization obtained for Beam 2 is smaller compared to Beam 1. Since the degree of linear polarization is equal for both beams, this indicates a slight misalignment in the beamline, e.g. due to the first quarter-wave plate. For both beams, a degree of polarization greater than 99% is desired, which is currently only achieved by Beam 1.

### Beam Pointing Stability

To ensure consistent count rates of the backscattered photons, the electron beam should constantly be hit by the photon beams. Thus a quantity of interest is the beam pointing stability, i.e. the transverse beam position over time. This is measured using the *ModeMaster PC*'s pointing stability measurement. The reference plane is at the end of the vacuum beamline, roughly 3.5 m distant from the interaction region. During each measurement, the ModeMaster determines the transverse beam position and orientation every 200 ms. The total duration of each measurement was chosen to be 120 s. Switching the quarter-wave plates is accompanied with certain concussions. To observe the effect of these concussions on the beam stability, the quarter-wave plates have been switched every 20 s for the second half of the measurement. The resulting maximum position deviations are shown in Table 3.8. For Beam 2, a significantly higher vertical instability is apparent.

At the reference point of the measurement, the beam pointing instabilities are one order of magnitude below the respective beam diameter  $\omega_e$  given in Table 3.6. Compared to the beam diameters in the interaction region  $\omega_0$ , the transverse instabilities are still significantly smaller than the beams themselves. Since the electron beam exceeds both laser beams in size, it can be concluded, that the transverse beam stability is sufficient for compton polarimetry.

	Beam 1	Beam 2
$\Delta x / \text{mm}$	$0.16 \pm 0.03$	$0.23 \pm 0.04$
$\Delta y / \text{mm}$	$0.15 \pm 0.03$	$0.35 \pm 0.04$

Table 3.8: Transverse beam instabilities of the MonoDisk laser system at the end of the vacuum beamline.

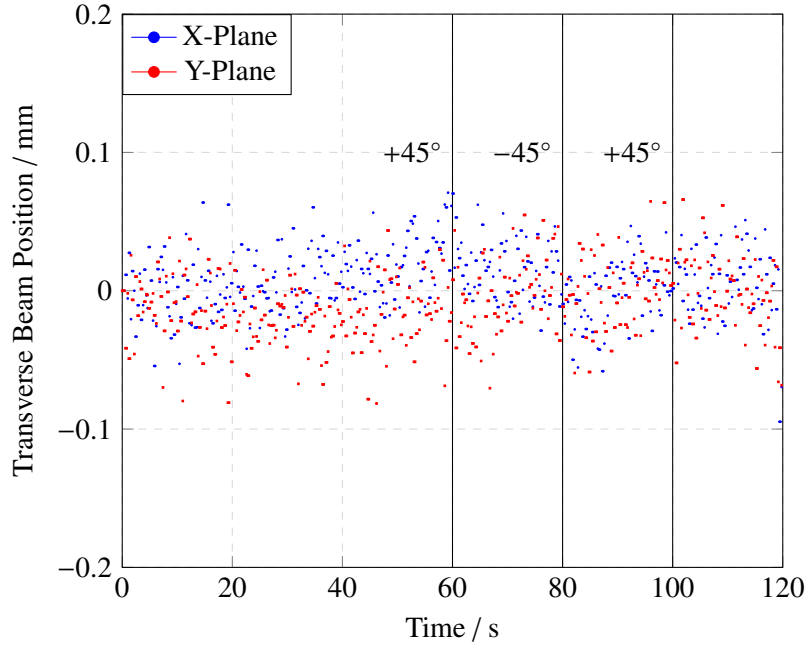


Figure 3.21: Beam pointing stability at the end of the vacuum beamline for Beam 1.

### 3.4 Polarization Measurement Station

The last section of the Compton beamline is the polarization measurement station, pictured in Fig. 3.23. It is mounted on an aluminum pipe filled with concrete and lead pellets for structure-borne sound insulation. All supply connections are located underneath the base. On this base, two identical measuring tables, as shown in Fig. 3.24, are mounted.

These tables are each mounted on two crossed precision linear stages<sup>1</sup> driven by 24 V DC-engines. The engines are controlled by a PLC<sup>2</sup> system and can be operated from the ELSA control system.

The circularly polarized portion of the light beam passes through a second quarter wave plate, fixed at an angle of  $-45^\circ$ , leading to linearly polarized light: Depending on the previous handedness of circular polarization, this portion of light is then fully *s*- or *p*-polarized. A polarizing beamsplitter separates these two components. A following intensity measurement is used to determine the degree of circular polarization of the laser beam using the principle already applied in section 3.3.5.

Instead of the primary beam, transmissions through the dielectric mirrors are used for the intensity measurement. The principle setup is shown in Fig. 3.25. As was mentioned, the reflectivity of a dielectric surface depends on the polarization of the incident light. This is nullified by the orientation of the mirrors following the beamsplitters, each deflecting in the *s*- or *p*- direction only.

<sup>1</sup> Owis: LTM 60-25 HSM

<sup>2</sup> Programmable Logic Controller

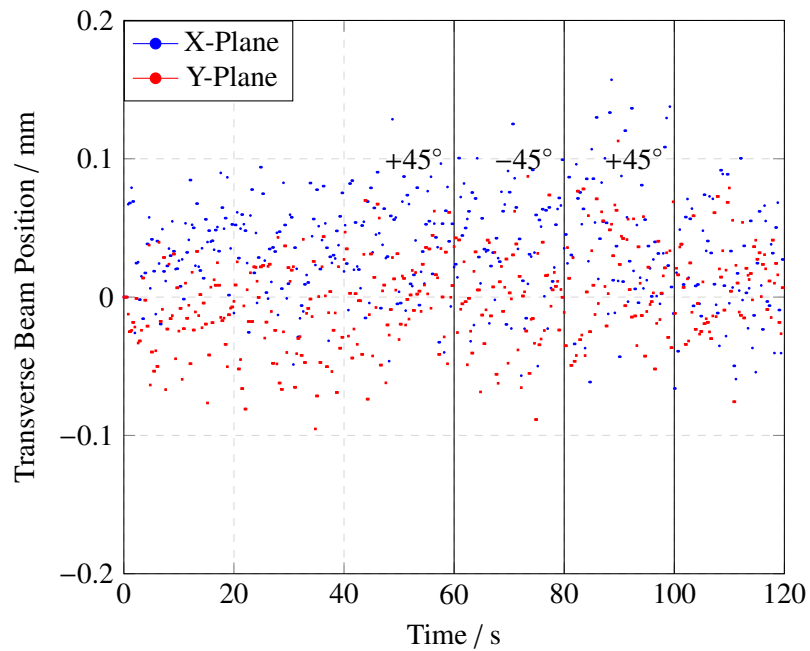


Figure 3.22: Beam pointing stability at the end of the vacuum beamline for Beam 2.

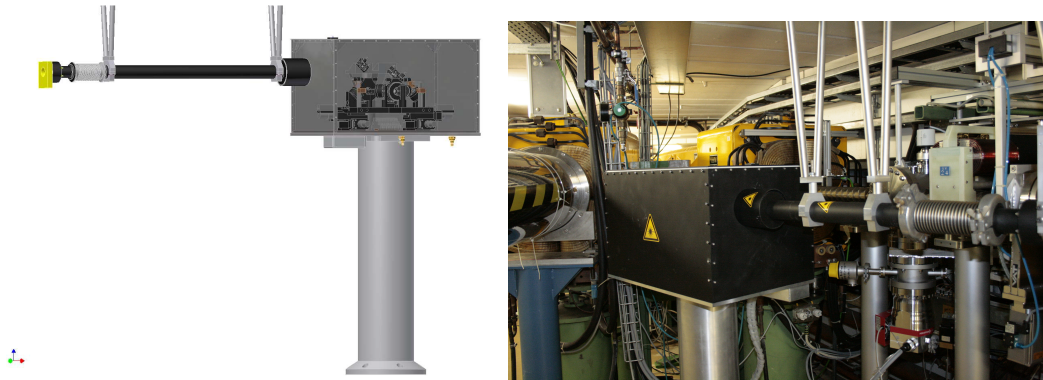


Figure 3.23: The polarization measurement station in its current state. CAD model taken from [4].

Finally, the laser beams are dumped in small copper blocks connected to water loads.

To protect the electronics from synchrotron radiation, the measurement tables are set up 23 cm below the accelerator plane [4]. The laser beams are deflected within this setup using dielectric mirrors. As additional diagnostic, a CCD camera has been placed<sup>3</sup> behind the vertically deflecting mirror in the path of beam 1. This camera is read out by a framegrabber card whose signal can be displayed on the monitor array in the control room. The beam position and shape can be observed at any beam power above roughly  $100\mu\text{W}$ , even allowing for conclusions concerning the mode composition of the beam. A similar setup is intended to be implemented for Beam 2 in the future.

<sup>3</sup> Provided by M. Switka

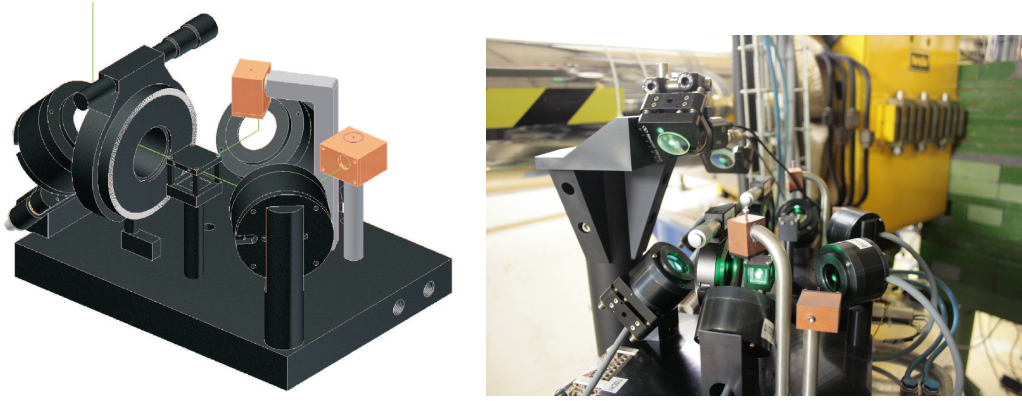


Figure 3.24: CAD model of the polarization measurement tables as documented by [4]. The photograph shows the current state with the CCD camera installed behind the vertically deflecting mirror.

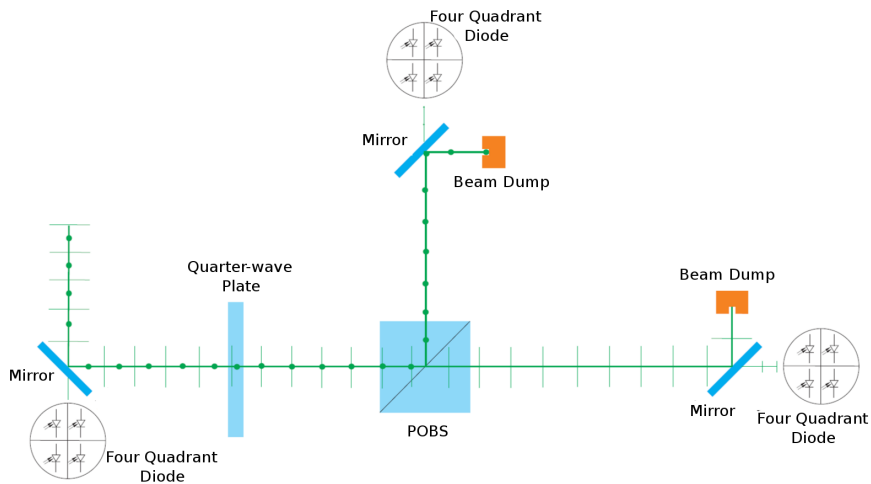


Figure 3.25: The operation principle of the photon polarization measurement station [4].

### Four Quadrant Photodiodes

The transmitted intensity is measured using four quadrant photo diodes placed below each deflecting mirror on the measurement tables. These diodes can also be used to determine the laser beam's transverse position. The beam intensity is given by the sum signal  $U_{\text{sum}} = U_1 + U_2 + U_3 + U_4$  of all four quadrants.

The four quadrant diodes also allow for a position measurement of the laser beam. The horizontal position  $X$  and vertical position  $Y$  are obtained by

$$X = \frac{(U_1 + U_3) - (U_2 + U_4)}{U_{\text{sum}}} \quad Y = \frac{(U_1 + U_2) - (U_3 + U_4)}{U_{\text{sum}}}. \quad (3.2)$$

Each quadrant is connected to an operational amplifier, schematics are shown in Fig. 3.26. The amplified signals are transported over a distance of roughly 20 m to the control PC in the experimental area. A low-pass filter is installed in order to reduce signal noise. The signal is then digitized using an ADC card built into the control PC.

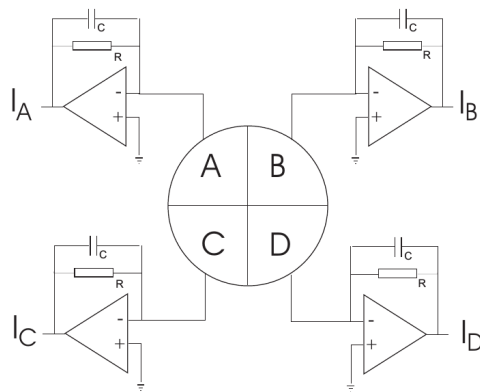


Figure 3.26: Schematics of the four quadrant photodiodes used including the operational amplifier [4].

As of now, the obtained signal does not allow for any quantitative measurement. In the future, the readout of the photo diodes will be performed using single board computers in order to achieve better signal qualities compared to the current setup.

---

## Summary and Outlook

---

During this work, the laser beamline at the Compton polarimeter at ELSA was successfully set up and characterized. This was accomplished by numerous studies of the laser system's performance and properties. A simple program can now be used to operate the laser system. First measurements with the detector system could be performed.

The laser system proved to be unable to provide the design total output power of 40 W following several repairs of the resonator in the past. The typically obtained output power varied from 25 W to 30 W. The power stability on the timescale of seconds is considered to be acceptable for Compton polarimetry at ELSA.

The beam properties of both beams were determined using the ModeMaster that bases its calculations on a four cuts measurement. For low intensities, the laser system's beam propagation factor remained within the manufacturer's specifications  $M^2 \leq 1.1$ . For higher output powers however, the beam propagation factor increased to values  $M^2 \leq 2$ , which has negative impact on the achievable beam waist and depth of focus. This was found to be caused by dynamics inside the laser's resonator, such as mode hopping. A CCD camera installed in the beamline is able to resolve the different modes dominating the laser's intensity distribution by monitoring the transverse intensity profile transmitted through a dielectric mirror. This *mode beating* causes intensity noise on timescales of milliseconds and below. This noise is not expected to have severe impact on the polarization measurement.

Using the beam properties obtained from the ModeMaster measurements, a focusing telescope setup was installed for both beams. These telescopes focus the beams in the interaction region in 16 m distance. The depth of focus covers the entire interaction region. Within this region, the width of both beams exceeded the electron beam width. The transverse beam pointing stability of the laser beams in the interaction region is sufficient for Compton polarimetry, being in the order of  $200 \mu\text{m}$ . Switching the photon polarization using the pneumatic quarter-wave plates caused no visible beam displacement. The degree of circular polarization obtained in the interaction region meets the aim of  $P_\gamma > 99\%$  for one of the two beams. For the second beam, the degree of circular polarization was found to be slightly lower. A readjustment of the quarter-wave plate in the pneumatic suspension should solve this issue.

With the detector system installed in the polarimeter, first tests and calibration measurements have been performed. As can be clearly seen in Fig. 4.1, the electron beam interacts with the laser photons, leading to a distinct signal above the background. In the future, some pending upgrades and additional studies can be performed to improve the beamline performance:

- The lenses used for the Beam 2 focusing telescope have to be substituted with AR-coated lenses.
- An additional CCD camera should be installed to monitor the intensity distribution of Beam 2.

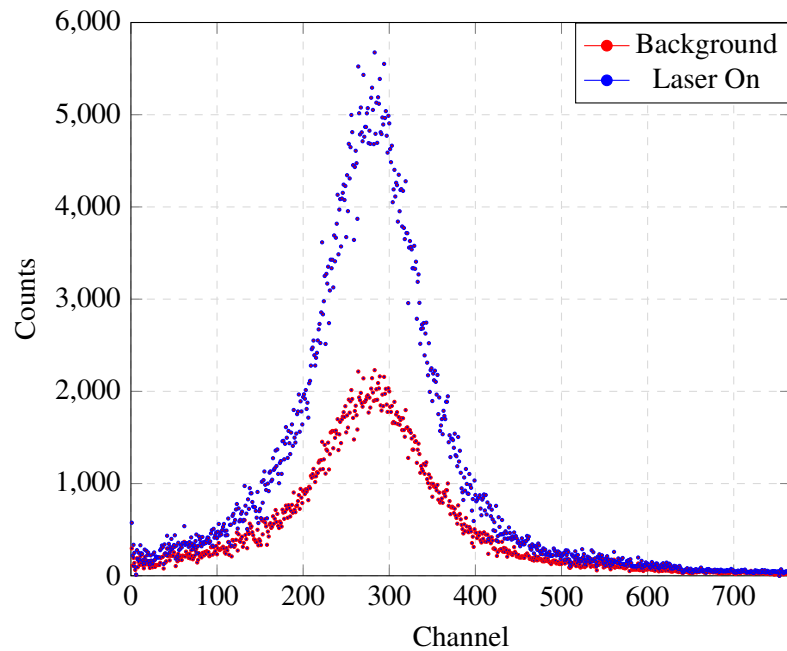


Figure 4.1: Profile of the backscattered photons as well as the background measured by the detector system. The signal caused by the backscattered laser photons significantly exceeds the background.<sup>1</sup>

- The pneumatic quarter-wave plate in the path of Beam 2 should be readjusted in order to obtain a higher degree of circular polarization.
- The four quadrant diodes in the polarization measurement station have to be recomissioned, allowing for continuous measurements of the laser beams' positions, intensity and degree of polarization. As of now, the signals obtained from the diodes are not suited for such measurements. Ongoing improvements of the read-out is expected to solve this issue.

Following a completed calibration of the detector system, first attempts for polarization measurements in storage mode can be performed.

---

<sup>1</sup> Courtesy of R. Koop.

# Bibliography

---

- [1] Althoff, K.H. “The 2.5 GeV Electron Synchrotron of the University of Bonn”. In: *Nuclear Instruments and Methods* 61 (1967), pp. 1–30.
- [2] Doll, D. “Das Compton Polarimeter an ELSA”. PhD thesis. 1998.
- [3] A. H. Compton. “A Quantum Theory of the Scattering of X-Rays by Light Elements”. In: *Physical Review* 21 (1922).
- [4] B. Aurand. “Die Laserstrahlführung des neuen Compton-Polarimeters an ELSA”. MA thesis. 2008.
- [5] Jackson, J.D. *Classical Electrodynamics*. 4th ed. de Gruyter, 2004.
- [6] Lipps, F.W. and Tolhoek, H.A. “Polarization Phenomena of Electrons and Photons: I”. In: *Physica* 20 (1954), pp. 85–98.
- [7] Sokolov, A. and Ternov, L. “On Polarization and Spin Effects in the Theory of Synchrotron Radiation”. In: *Soviet Physics-Doklady* 8 (1964), pp. 1203–1205.
- [8] A. et al. Giesen. “Scalable Concept for Diode-Pumped High-Power Solid-State Lasers”. In: *Applied Physics B: Lasers and Optics* 58 (1994), pp. 365–372.
- [9] Franken, P.A. et al. “Generation of Optical Harmonics”. In: *Physical Review Letters* 7 (1961).
- [10] Nikogosyan, D.N. “Lithium Triborate (LBO), A Review of its Properties and Applications”. In: *Appl. Phys. A* 58 (1994), 181f.
- [11] M.C. Teich and B.E.A. Saleh. *Grundlagen der Photonik*. Wiley-Vch, 2008.
- [12] A.E. Siegman. “Hermite-Gaussian Functions of Complex Argument as Optical-Beam Eigenfunctions”. In: *Journal of Optic A: Pure and Appl. Opt.* 19 (1973), 1093f.
- [13] F. Hinterberger. *Physik der Teilchenbeschleuniger und Ionenoptik*. Springer, 2008.
- [14] Johnston, T.F. “Beam propagation ( $M^2$ ) measurement made as easy as it gets: the four-cuts method.” In: *Applied Optics* 21 (1998), pp. 4840–4850.
- [15] International Organization for Standardization. “ISO 11146 Lasers and laser-related equipment – Test methods for laser beam widths, divergence angles and beam propagation ratios”. In: *ISO Standards catalogue* (2005).
- [16] W. Demtroeder. *Experimentalphysik 2 - Elektrizität und Optik*. Vol. 5. Springer, 2009.
- [17] Coherent. *ModeMaster PC User Manual*.
- [18] Inc. Wolfram Research. *mathematica*. 10.3. Wolfram Research, Inc., 2015.



# List of Figures

---

1.1	Schematics of the Electron Stretcher Accelerator ELSA. . . . .	2
2.1	Nomenclature of Compton scattering [4]. . . . .	3
2.2	Cross section for scattering a photon off a free electron in the electron's rest frame. . .	5
2.3	The cross section for Compton scattering in the electron's rest frame for circularly polarized photons and linearly polarized electrons. . . . .	7
2.4	Modulation depth in dependance of the scattering angle $\theta^*$ for different incident photon energies. . . . .	8
2.5	Design of the Compton polarimeter at ELSA with key components: A laser system (a), beam shaping optics (b), beamline with the interaction region (c), photon polarization measurement station (d) and a detector system (e) for the measurement of backscattered $\gamma$ -photons. This sketch is not true to scale. . . . .	9
2.6	Concept of a disk laser unit. [4] . . . . .	10
2.7	Interior setup of the ELS MonoDisk Gemini 20 disk laser. [4] . . . . .	12
2.8	Parameters of a Gaussian beam . . . . .	14
2.9	Depiction of the four-cuts method. . . . .	16
2.10	Reflectance of $s$ - and $p$ - polarized light at the boundary between air and fused silica, depending on the incident angle. . . . .	18
2.11	Reflectance of $s$ - and $p$ - polarized light at the boundary between fused silica and air, depending on the incident angle. . . . .	19
2.12	Phase shift between $s$ - and $p$ -polarized light depending on the incident angle for total internal reflection at the boundary between fused silica and air. . . . .	20
3.1	CAD model of the optical table. [4] . . . . .	22
3.2	The optical table in its current state. The detector system is already in place on the rear end of the uppermost plate. . . . .	23
3.3	Sketch of the laser beams in the beamline. [4] . . . . .	24
3.4	The Compton beamline in the ELSA tunnel. The optical beamline enters the electron beampipe in the M25 magnet and leaves the stretcher ring in the M24 magnet. . . . .	25
3.5	Sketch of the <i>ModeMaster PC</i> Beam Propagation Analyzer according to [17]. . . . .	26
3.6	The intensity profiles used for both beam diameter measurement techniques as found in [17]. The $x$ -axis is scaled with the beam width $w$ . For the knife-edge measurement, the principle of different clip levels and width adjustment factors is shown. . . . .	27
3.7	Output power of both laser beams depending on the pumping diode current for two successive ramps. . . . .	31
3.8	Laser output power in dependance of the time passed. After about 5 min, the maximum pumping current $I_{Set} = 60$ A was reached. . . . .	32
3.9	Output power in dependance of temperature changes measured on the laser's casing. .	32

3.10	Photo diode response to the adjustmend laser diode and the MonoDisk laser. . . . .	33
3.11	Pump diode power in dependance of the pumping current. . . . .	33
3.12	Pump diode power in dependance of the passed time for a pumping current $I_{Set} = 60$ A. . . . .	34
3.13	Mode hops resolved using a CCD camera. The dominant mode of the laser beam switches from the TEM <sub>00</sub> -mode to the TEM <sub>01*</sub> -mode. . . . .	35
3.14	Sketch of the setup used to determine the degree of linear photon polarization provided by the MonoDisk laser system. . . . .	36
3.15	Linearly polarized intensity in dependance of the total incident intensity. The degree of polarization is given by the ratio of both values. . . . .	37
3.16	Adjusted beam propagation in the vacuum beam line for an electron beam energy of 3.2 GeV. The ModeMaster was placed at $z = 0$ . . . . .	40
3.17	Adjusted beam propagation in the vacuum beam line for an electron beam energy of 1.7 GeV. The ModeMaster was placed at $z = 0$ . . . . .	40
3.18	Sketch of the setup used to measure the photon beam's degree of circular polarization. . . . .	41
3.19	Measurement of the circular degree of polarization of Beam 1. . . . .	41
3.20	Measurement of the circular degree of polarization of Beam 2. . . . .	42
3.21	Beam pointing stability at the end of the vacuum beamline for Beam 1. . . . .	43
3.22	Beam pointing stability at the end of the vacuum beamline for Beam 2. . . . .	43
3.23	The polarization measurement station in its current state. CAD model taken from [4]. . . . .	44
3.24	CAD model of the polarization measurement tables as documented by [4]. The photography shows the current state with the CCD camera installed behind the vertically deflecting mirror. . . . .	45
3.25	The operation principle of the photon polarization measurement station [4]. . . . .	45
3.26	Schematics of the four quadrant photodiodes used including the operational amplifier [4]. . . . .	46
4.1	Profile of the backscattered photons as well as the background measured by the detector system. The signal caused by the backscattered laser photons significantly exceeds the background. . . . .	48

# List of Tables

---

3.1	The beam properties obtained by the <i>ModeMaster PC</i> . . . . .	27
3.2	Beam parameter measurement with the adjustment laser diode. For the first measurement, the distance diode-ModeMaster was 0.76 m, for the second measurement 1.71 m. The results are given for both transverse planes as well as the <i>rad</i> -mode of the respective beam. . . . .	29
3.3	Beam parameter measurement for both laser beams. The distance between the ModeMaster and the Laser was 1 m. . . . .	30
3.4	Degree of linear polarization in <i>s</i> -direction of the ELS MonoDisk laser beams. . . . .	36
3.5	Possible combinations of lenses fulfilling the desired conditions, sorted by the waist size in the interaction region. The telescopes currently used are highlighted. . . . .	38
3.6	Measured properties of the adjusted MonoDisk laser beams. The distance between the ModeMaster and the interaction region is given by $d_1 = 3.658$ m and $d_2 = 3.788$ m. The results are given for both transverse planes as well as the <i>rad</i> -mode. . . . .	39
3.7	Degree of circular polarization of the MonoDisk laser beams obtained in the vacuum beamline. . . . .	41
3.8	Transverse beam instabilities of the MonoDisk laser system at the end of the vacuum beamline. . . . .	42



# Acknowledgements

---

Ich möchte mich an dieser Stelle bei allen bedanken, ohne die die Erstellung dieser Arbeit nicht möglich gewesen wäre. Mein besonderer Dank richtet sich an

- Herrn PD Dr. Wolfgang Hillert, der jederzeit zur Beantwortung von Fragen und für Hilfestellungen zur Verfügung stand.
- Herrn Prof. Dr. Jochen Dingfelder für die Übernahme des Koreferats.
- Meinen Bürokollegen Michael Switka, Rebecca Koop, Daniel Kuckla und Tobias Schiffer für die stets heitere Arbeitsatmosphäre und die vielen, konstruktiven Diskussionen.
- Michael Switka und Rebecca Koop für die zahllosen Hilfestellungen während dieser Arbeit.
- Rebecca Koop, Michael Switka, Dennis Proft und Dennis Sauerland für das Korrekturlesen dieser Arbeit.
- die ganze ELSA-Arbeitsgruppe, für die wunderbare Zeit mit euch.
- meiner Familie, für all die Unterstützung in den vergangenen Jahren, die mir dieses Studium erst ermöglicht haben.

Auch an alle, die hier nicht erwähnt wurden, nochmal ein herzliches

**DANKE!**